AN INTERACTIVE COMPUTER GRAPHICS SYSTEM FOR 3-D STEREOSCOPIC RECONSTRUCTION FROM SERIAL SECTIONS: AN APPLICATION IN THE STUDY OF PULMONARY METASTATIC GROWTH

by

SUNIL DUTT CHAWLA

A Thesis submitted to the Faculty of Graduate Studies and Research in partial fulfillement of the requirements for the degree of Master of Engineering.

Department of Electrical Engineering
McGill University
Montreal

March 1979

COMPUTER AIDED RECONSTRUCTION OF SERIAL SECTIONS

to my parents

and

my sister

AN INTERACTIVE COMPUTER GRAPHICS SYSTEM FOR 3-D RECONSTRUCTION FROM SERIAL SECTIONS: AN APPLICATION IN THE STUDY OF PULMONARY METASTTIC GROWTH

Sunil Dutt Chawla M.Eng. Thesis
Dept. of Electrical Engineering
McGill University

ABSTRACT

This treatise describes research to date on a computer based system for the analysis of the growth of pulmonary metastatic tumors. The computer system permits:

1. Data acquisition of serial sections.
2. Assembly (alignment) of serial sections to store a 'computer model' of the lung.
3. Three dimensional stereoscopic display of the lung on a storage tube terminal.
4. Computation of the volume and surface area of the tumor nodules in the lung. The inter-nodule distance matrix can also be computed.
5. Simulation of the three-dimensional random pattern of growth of tumor nodules in the lung.

Serial sectioning artifacts hampering reconstruction of metastatic growth have been identified and connected.

Experiments were conducted to study the growth of metastatic tumors in mouse lung. The computer system was used to reconstruct the lungs under study and perform quantitative analysis.

Evidence, indicates, that the three dimensional spatial distribution of tumor nodules in mouse lung may be non-random.

There were wide differences in the size of tumor nodules in the individual lungs as well as in different lungs. The size of perenchymal tumor nodules was much smaller than the size of peripheral tumor nodules.

The computer software developed by us represents an important methodological breakthrough in the field of experimental oncology.

RESUME

Cette thèse décrit le travail fait jusqu'à ce jour sur un système computérisé d'analyse de la croissance des nodules de tumeurs pulmonaires. Ce système assisté par ordinateur permet:

1. L'acquisition des données décrivant des sections pulmonaires successives.
2. L'assemblage (et l'alignement) de sections successives aux fins de stockage d'un modèle computérise des poumons.
3. La reproduction d'images sténéoscopiques tri-dimensionelles des poumons sur écran graphique a mémoire.
4. Le calcul du volume et de l'aire de la surface des nodules dans les poumons. La matrice des distances inter-nodulaires peut aussi être calculée.
5. La simulation de patrons tri-dimensionelles de la croissance des tumeurs dans les poumons.

Les distorsions introduites dans la reconstruction des images par les artéfacts provenant du découpage ont été identifiés et corrigés.

Des expériences ont été realisées pour étudier la croissance des tumeurs au stade de la métastase dans les poumons de la souri. Le système assisté par ordinateur fut utilisé pour reconstruire les poumons etudiés et pour effectuer des études quantitatives.

Les resultats de cette étude indiguent que la distribution tri-dimensionelle des nodules n'est pas uniquement aléatoire.

Des differences importantes furent trouvées dans les dimensions des nodules localisés dans un poumon ou dans des poumons différents. La taille des nodules de tumeurs parenchymales était beaucoup plus petite que la taille des nodules périphériques.

Le logiciel developpé aux fins de cette étude représente une percée méthodologique importante dans le domaine de l'oncologie expérimental.

ACKNOWLEDGMENTS

My sincere thanks are due to Dr. Leon Glass for his expert guidance of this project.

I am grateful to Dr. Julian Proctor, Allegheny General Hospital, Pittsburgh for the benefit of many fruitful discussions. He undertook the inoculation of the mice with tumor cells and the histological preparation of the excised lungs.

The lungs were serially sectioned, stained and mounted on microscopic slides by Mr. Marcel Antos of the Dept. of Pathology, McGill University.

Professor A. S. Malowany greatly assisted in the graphics display aspects of the computer system. I benefited immensely from his sage counsel.

The Biomedical Engineering Unit Computer Staff responded promptly to our many needs and provided excellent support.

Mr. Lee Foon assisted in constructing a plexiglass model of the lung.

I also am grateful to Gino Petrillo for tangible moral encouragement.

Brian Hanna smilingly undertook the arduous task of correcting the typescript.

This research was funded by the Cancer Research Society of Montreal.

I wish to thank McGill University for awarding me the Alexander McKee Fellowship.

I am deeply indebted to them all.

CONTENTS

CHAPTER I

INTRODUCTION

1.1 Metastatic Growth.

Metastasis is the dissemination and growth of cells released from a primary tumor . The metastatic process begins with the separation of cells from a primary tumor followed by dissemination, initial establishment and proliferation of the released cells (25,42).

There have been several studies of the initial steps of hematogenous dissemination of cancer cells in animal models (3,7,42,47). It has been possible to analyze quantitatively the arrest of tumor cells in capillary walls of vascular beds , and the ability of these cells to traverse the capillary walls to initiate tumor nodules(10,24,25,26,48). The proliferation of arrested tumor cells is dependent on factors of nutrition and a variety of host factors including tumor angiogenic factor (12), tumor blood supply (11,16,42,46), immune response (29). The control of vascularization of tumor nodules, as well as the possible interaction between the vascular supply and other local environmental factors which may influence tumor growth are poorly understood(7,9,32).

I have studied the three dimensional spatial distribution of tumor nodules in mouse lung produced by intravenous inoculation of tumor cells. Evidence strongly indicates that the spatial distribution of tumor nodules in mouse lung is non-random. The pattern of growth can elucidate the processes involved in the growth of tumors.

1.2 Quantitative Methods.

The number and size of tumor nodules are essential parameters in the quantitative analysis of factors affecting metastatic growth. Quantitation of these parameters can provide invaluable information in the assessment of various treatment modalities, such as radiation therapy, chemotherapy etc. Such determinations are necessary in the analysis of kinetics of tumor growth (37,39) and immune response (4,29) to metastatic growth.

A systematic analysis of all serial sections of an organ (with dispersed tumor nodules) is necessary to determine the number and size of the tumor nodules. Since the counting and sizing of tumor nodules is laborious, several investigators have developed approximation techniques.

Wexler (43), in conducting experiments on mouse lung, injected India ink into the trachea to identify pulmonary metastases. Tumor nodules on the surface of the lung were observed with the naked eye or with the aid of a lens. Tumor nodules not on the surface of the lung were ignored.

Lucke et al. (28) sectioned the livers and lungs of rabbits into slices 2mm thick and examined the metastases. The largest diameter of the tumor nodule was recorded and

the volume of an equivalent sphere computed. It is likely that extremly small tumors may have escaped detection.

Nelligren and Boeryd (4) adapted a method developed by Wicksell (44,45) to quantitate the number and size of any structures (such as tumor nodules) in an organ (such as the lung). Their method involves the examination of a limited number of sections cut at arbitrary levels through the organ. On the assumption that the tumor nodules are spherical (or ellipsoids) and that they are uniformly distributed throughout the organ , empirical formulae were developed to quantitate the number and size of metastases.

Khato et al. (19) used the method developed by Nelligren and Boeryd (4) to quantitate the number and size distribution of metastases in lungs of rats. Wood et al. (46) used a method developed by Zeidman et al. (47) to study the relationship between metastatic tumor size and the number of lung metastases.

The initial 'seeding' of tumor nodules is considered non-random for many types of malignant cells (31). Also, it has been found that most pulmonary metastases are located on or near the surface of the lungs (29). Consequently, available quantitative methods could lead to systematic errors and erroneous interpretations since the methods are based on

on assumptions that may not be tenable.

It is necessary to collect systematic data concerning growth of metastatic tumor nodules in an attempt to analyze the control mechanisms regulating growth. I have developed a computer based system to reconstruct an organ from its serial sections. The number and size of tumor nodules may be ascertained correctly. In addition , a three dimensional color stereoscopic display of the lung may also be obtained. This system enables us to carry out studies relating to the growth of tumor nodules.

1.3 Three Dimensional Reconstruction Techniques.

Biologists have performed three dimensional reconstructions of structures from serial sections for over a century (14). Early efforts usually resulted in the preparation of physical models or artists' drawings of the structures under study; or outlines of the serial sections were drawn on transparent sheets. It is difficult to obtain quantitative information from such reconstructions.

Several investigators (13,20,22,23,33,35) have turned to computer techniques of reconstruction from serial sections. Levinthal et al. (22,23) used computer reconstruction techniques to display neurons and their branching pat-

terns in the central nervous system of the water flea, Daphnia. Reddy et al. (35) describe a computer system for the reconstruction and analysis of neuronal structure using the specific example of the lobster swimmeret system.

Reconstruction of three dimensional structures from serial sections involves display of three dimensional information on a two dimensional plane . A variety of techniques can be used for this purpose (30). The simplest technique is to display several orthogonal views such as the plan , elevation and sectional drawings. However, it is difficult to conceive complicated structures from such views.

Another alternative is perspective view display. Different types of perspective views can be displayed, viz. wire-frame , outline and shaded views. Each of these techniques produces a different visual effect.

To simulate depth in three dimensional pictures, depth cues can be provided in various ways. Removal of hidden lines or hidden surfaces is very effective. Intensity cues, kinetic depth effect , and stereoscopic effect are some of the other techniques used to furnish depth cues.

Stereoscopic views produce an excellent three dimensional effect. Two perspective views of the object are

drawn: one view for the left eye and another for the right eye. The perspective views are generated appropriate to the location of each eye. The view corresponding to each eye can be directed to the appropriate eye by means of stereoscopic viewers. Fusion of the two images in the brain results in a three dimensional visualization of the object.

Stereoscopic displays (stick models) have been extensively employed in the study of the molecular structure of organic molecules (5,21). Wire-frame stereoscopic pictures are commonly drawn by topographers.

Nevertheless, to the best of my knowlwdge, wire-frame stereoscopic display of reconstruction from serial sections has not been attempted. I have developed an interactive computer graphic system (Lung System) to reconstruct an organ (containing different structures within) from its serial sections. Stereoscopic wire-frame pictures of the reconstructed organ can be displayed on a storage tube terminal. In the following chapters, I present details on various aspects of software developed for this system.

Chapter II introduces the Lung System. I describe the data acquisition system and programs written to transcribe pertinent data from histological slides to the data base on the storage disk.

In Chapter III, I develop the algorithm to perform the alignment operation on the histological slides. Algorithms to carry out the necessary transformations on the data base to display the stereoscopic images (on a storage tube terminal) are described. Algorithms to extract quantitative data such as volume and surface area of tumor nodules are also presented.

Finally, Chapter IV describes experiments conducted to study the growth of tumor nodules in the upper left lobe of mouse lung. Quantitative data required for the analysis of these experiments was obtained with the aid of the Lung System.

CHAPTER II

THE LUNG SYSTEM

2.1 Introduction.

This Chapter presents an overview of the Lung System. Its functional requirements are first defined. The operating environment consisting of the computer hardware and system software are detailed. The principles underlying data acquisition and the data base, consisting of the primary and secondary files are described.

2.2 Overview Of The Lung System.

Lung is the Computer System Software being developed at the Biomedical Engineering Unit, McGill University, for the three- dimensional reconstruction of stain injected mice lung with metastatic tumor nodules. To achieve the goals implied in our research objectives (Chapter I), this system must meet several functional requirements. Specifically, it must:

1. accept and store the outlines of the lung, tumor nodules and the alignment marks in the sections;

2. assemble all the sections of the lung together to generate a compact three-dimensional model of the lung and the tumor nodules;

3. display the lung on a cathode ray tube (CRT) or other output devices at any specified viewing angle;

4. extract required quantitative information on the various structures in the sections;

5. provide easy access to a novice user by means of interactive preprogrammed instructions.

The organization of the functional units with respect to the data base is depicted in fig.2.1. Each functional unit is logicaly independent of the other and operates on the data base. All programs concerned with data acquisition result in the generation of a compact data base.

The Lung System, as it stands today meets all the stated requirements. The system is interactive, ensuring user control at every crucial stage.

2.3 Computer System Hardware And Software.

The Lung System is implemented on a PDP-11/70 midicomputer with 256K bytes of core storage and 88M bytes of on-line mass storage (DEC RP04). Off-line mass storage consists of IBM-compatible floppy disks. The organization of the midicomputer and its peripherals is displayed in fig.2.2.

High speed Tektronix 40xx storage tube terminals are used for the display of three-dimensional pictures. Permanent copies of these pictures can be obtained on a graphics hard copier (Tektronix 4631). Colored pictures may be obtained on the digital plotter (Tektronix 4662).

The 'Input Station' consists of a Numonics Digitizer

Fig. 2.1. Every module is logically independent of the other and acts on the data base separately.

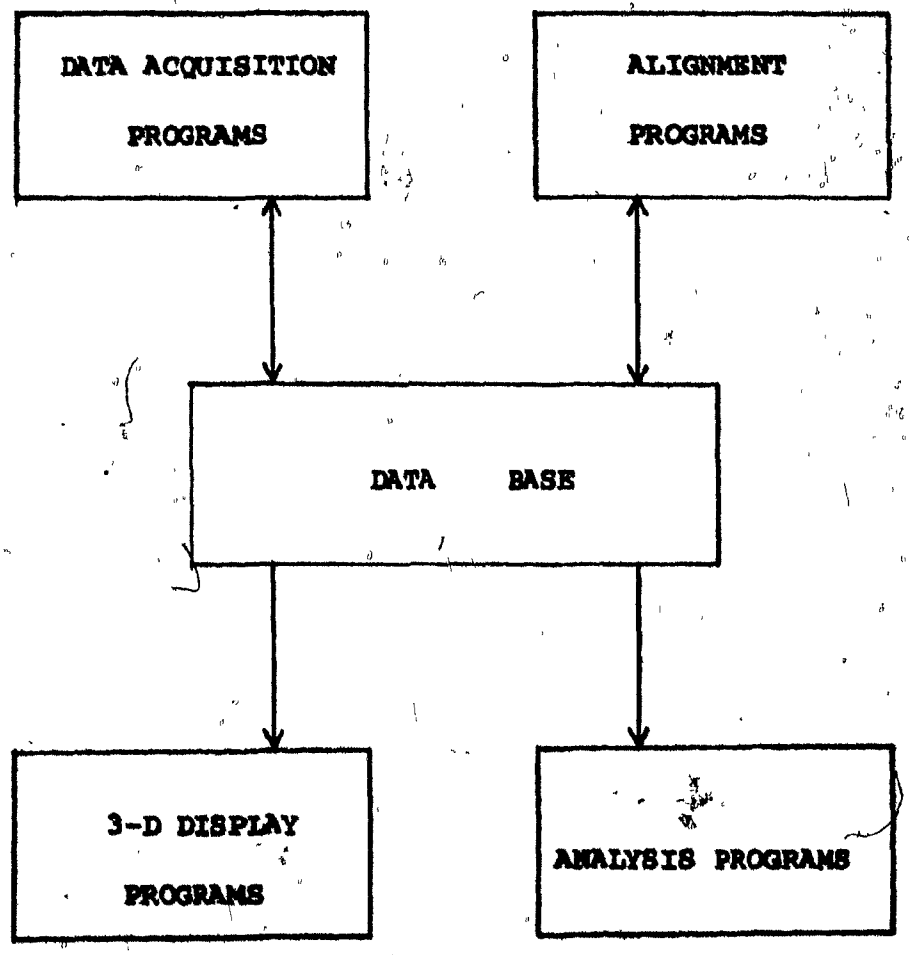

Organization of Lung System Software Modules with respect to the Data Base

Fig. 2.2. The Numonics Digitizer is connected to the PDP-11/70 through a serial interface. The Digital Plotter (Tektronix 4662) can be used to obtain colored pictures. The Xerox Hard Copier furnishes permanent copies of the storage tube displays.

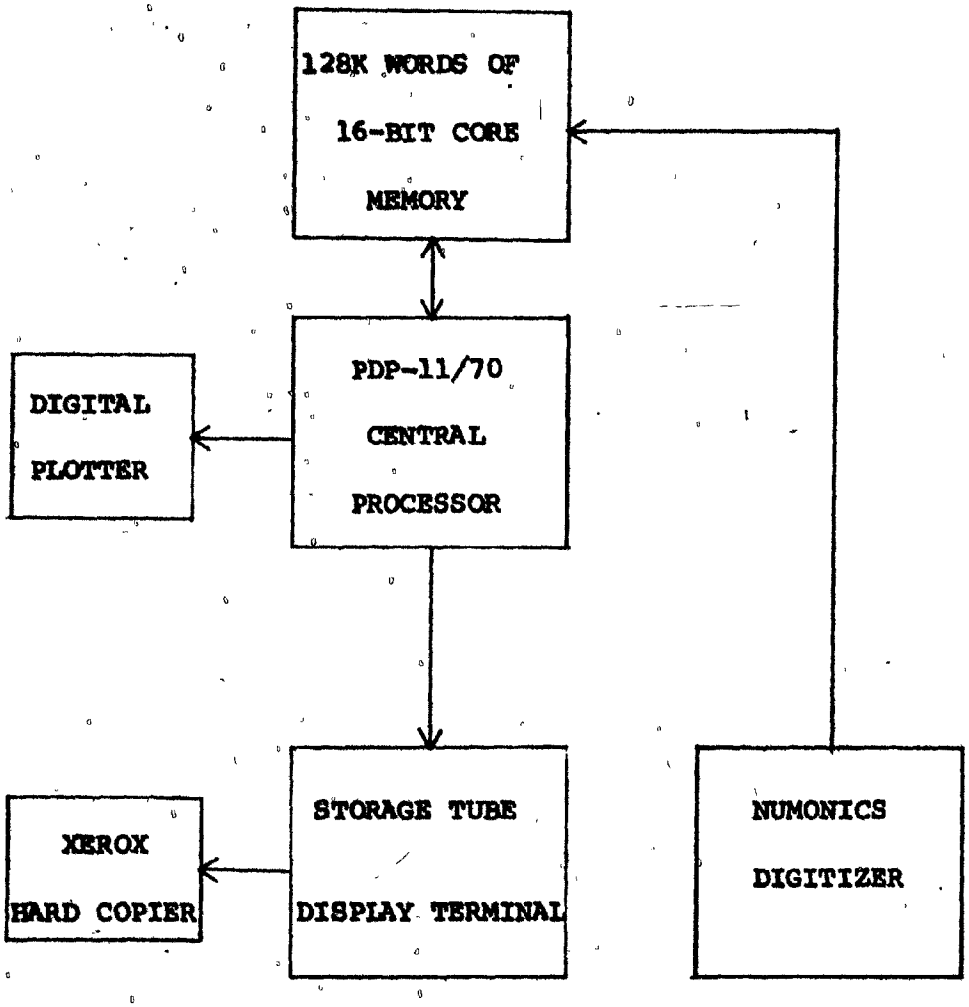

THE PDP-11/70 MINICOMPUTER AND ITS PERIPHERAL DEVICES

interfaced to the PDP-11/70 (fig.2.3). The slide to be digitized is mounted on the projector. The projector lens is adjusted so that a well focussed and magnified projection of the section is obtained on the Tablet. The outline of the contour may be traced using the 'pen' (the tip of the sliding arm). By pressing a button, the position of the pen is transmitted to the computer and displayed on the CRT to provide immediate feedback to the user.

The PDP-11/70 runs under the RSX-11M V03 Operating System in a real time multi-user environment. The Lung System is written in the PDP-11 FORTRAN IV PLUS language. DEC supplied graphics software package (PLOT-10) is used to direct graphic output to the storage tube terminals. The Scientific Subroutine Package (SSP) has also been used extensively.

2.4 Data Acquisition And Data Base.

The purpose of data acquisition is to extract relevant data from each section for use by the alignment and display programs. The relevant information consists of the boundary of the lung, tumor nodules and alignment marks in each section. The boundaries (or contours) of these structures are approximated by line segments, and internally represented as the coordinates of the end-points of the line segments.

Fig. 2.3. The histological slide is mounted on the projector. A magnified (27.36X) image of the contour on the tablet can be digitized. An instant display of the contour can be seen on the display terminal.

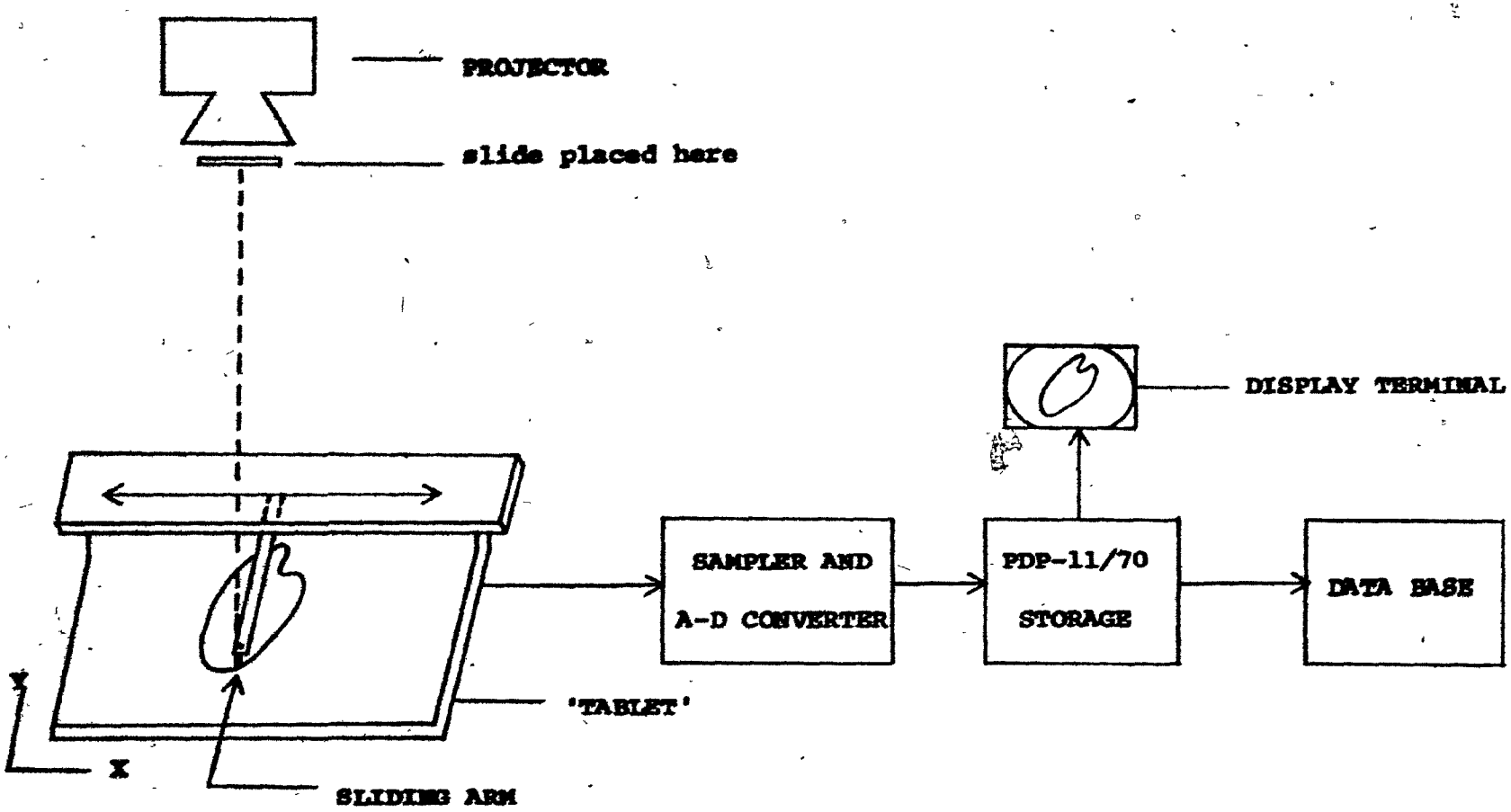

THE INPUT STATION

Data extracted from any lung is stored in two data files, viz. a primary data file and a secondary data file. The coordinates are stored in the secondary data file. The primary data file acts as a table of contents to the secondary data file by giving the address or location of all contours stored in the secondary file.

The primary data file is organized in terms of records. Each record being assigned to a specific structure (lung, tumor nodules or alignment marks). The record number explicitly identifies a structure. (For the sake of consistency the following numeral assignments have been chosen: record numbers 1 ,2 and 3 are assigned to the three alignment marks; record number 4 to the lung; and subsequent records are assigned to the tumor nodules.) A record, pertaining to a structure records the addresses of all contours composing it. Hence, the list of all contours in a structure can be conveniently 'read-off' from the secondary data file.

One record in the primary data file is reserved to store the Z-coordinate of all the sections composing the lung. In addition, the very first record in the primary data file contains information on the current status of digitisation. Complete details on the data structure of the primary and secondary data files are available in appendix A.

2.5 Storage Requirements.

A lung may be represented by no more than 64 serial sections. Accordingly, the primary data file is composed of records 64 words long (each word consisting of two bytes in the integer format). As shown in fig.2.4, 70 such records are available for use. The secondary data file is composed of 1000 records, each record being 32 words long (fig.2.5). Both the primary and the secondary data files exist as random access files on the system disk. The total information content of these two files amounts to a maximum of 73K bytes.

2.6 Data Acquisition Programs.

The Data Acquisition programs facilitate input of data and its subsequent routing to the proper location for storage in the data base. The programs set forth the interactive procedure in which the user may control the entry of data. At every stage, the data is checked for logical inconsistencies.

The programs concerned with data acquisition are: Program Data Acquisition, Program Display, Program Lung and Program Input. Program Connection is separately included to enable connections of the data base at any future time.

Fig. 2.4. The primary data file (random-access) consists of 70 records, each record containing 64 words. Tables named INFOR, MEMTAB, ZTAB, CONAD are stored in records as shown. Appendix A details the information content of these tables.

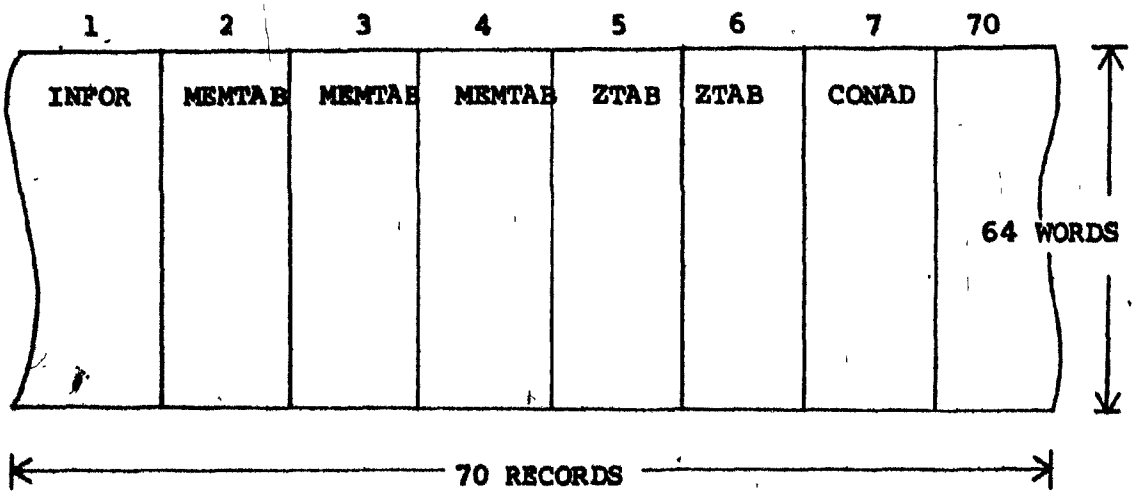

STRUCTURE OF THE PRIMARY DATA FILE

Fig. 2.5. The secondary data file (random-access) consists of 1000 records, each record containing 32 words. The X, Y coordinates of points along the contour are stored in this file in addition to information pertaining to a specific contour. The data structure is detailed in Appendix A.

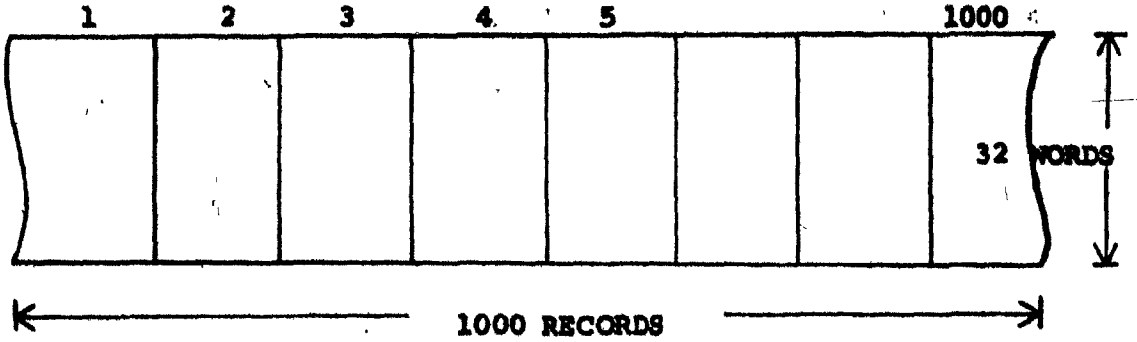

STRUCTURE OF THE SECONDARY DATA FILE

CHAPTER III

GENERATION OF THE THREE DIMENSIONAL MODEL

3.1 Introduction.

This chapter explains the alignment operation. The necessary transformations are developed. The principle of 3-D stereo display is presented. Algorithms to extract quantitative data such as volume and surface area of tumor nodules are presented.

3.2 Alignment Of Sections.

To generate a usable 'stored model' of the lung a preliminary alignment operation is necessary. The alignment operation must correct for variations in the positioning of the image of the section on the input tablet.

Two adjacent sections can be correctly aligned by matching up identical landmarks on the two sections. The landmarks can be the centers of the alignment contours and/or the centers of contours of other structures (lung and tumor nodules). The position of corresponding landmarks on the two sections is used to compute the displacement of one section relative to another in terms of a rotation (angle) and translation factor. Each of these factors is computed by applying the least squares criteria on the distance between the corresponding landmarks on the two sections. These transformations can be applied to all the contours composing the section being aligned. Repeating this procedure for all sections in the lung results in the generation of a compact model of the lung.

3.3 Translation And Rotation Factors.

Algorithms to compute the translation and rotation factors are based on the results of the following mathematical

development.

Let X_i and Y_i be the coordinates of the center of mass of the i th contour in the reference section. Also, let X_i' and Y_i' represent the coordinates of the center of mass of the i th contour in the section being aligned. If the section being aligned is moved by translation factors of A in the X-axis direction and B in the Y-axis direction, the resulting distance D_i between the corresponding landmarks can be expressed as:

$$D_i^2 = (X_i - (X_i' - A))^2 + (Y_i - (Y_i' - B))^2$$

The sum S of the square of these distances for N contours is expressed as:

$$S = \sum_{i=1}^{N} D_i^2$$

We are seeking A and B under the condition that S is minimized. Hence, we differentiate S with respect to A and B separately and set each of these differentials to zero. So,

$$\frac{dS}{dA} = 0$$

results in

$$2\sum_{i=1}^{N} (X_i - (X_i' - A)) = 0$$

giving

$$A = \frac{1}{N_1}\sum_{i=1}^{N}(X_i - X_i') \qquad 1a$$

Similarly, by setting

$$\frac{dS}{dB} = 0$$

we get

$$B = \frac{1}{N}\sum_{i=1}^{N}(Y_i - Y_i') \qquad 1b$$

Next, if the section being aligned is rotated by an angle α with respect to the reference section, the distance D_i between the corresponding landmarks can be expressed as:

$$D_i^2 = (X_i - (X_i'\mathrm{Cos}\alpha - Y_i'\mathrm{Sin}\alpha))^2 + (Y_i - (X_i'\mathrm{Sin}\alpha + Y_i'\mathrm{Cos}\alpha))^2 \qquad 2a$$

Once again, the sum S of the square of these distances for N contours is expressed as:

$$S = \sum_{i=1}^{N} D_i^2$$

Our aim is to find an angle α such that S is minimized. Hence, differentiating S with respect to angle α and setting the result to zero we get:

$$\frac{dS}{d\alpha} = 0$$

giving

$$\text{Tan}\alpha = \sum_{i=1}^{N} (Y_i X_i' - X_i Y_i') / \sum_{i=1}^{N} (X_i X_i' + Y_i Y_i') \qquad 2b$$

Alignment may be imperfect due to truncation and round-doff errors or due to imperfections inherent in the sections. This error may be defined as the average of the angle (in radians) each landmark is displaced relative to the reference section. The average error e is determined as follows.

In equation 2a, we saw that

$$D_i^2 = (X_i - (X_i' \text{Cos}\alpha - Y_i' \text{Sin}\alpha))^2 + (Y_i - (X_i' \text{Sin}\alpha + Y_i' \text{Cos}\alpha))^2$$

If alignment is perfect,

$$D_i = 0 \quad \text{for all } i.$$

Under this condition,

$$X_i = X_i' \text{Cos}\alpha - Y_i' \text{Sin}\alpha \qquad 3a$$

$$Y_i = X_i' \text{Sin}\alpha + Y_i' \text{Cos}\alpha \qquad 3b$$

Solving, 3a and 3b simultaneously, we get

$$\text{Tan}\alpha_i = (Y_i X_i' - X_i Y_i') / (X_i X_i' + Y_i Y_i')$$

where angle α_i is the angle the i th contour should be rotated to perfectly align it.

The average error e is therefore given by

$$e = \frac{1}{N}\sum_{i=1}^{N}(\mathrm{Tan}\alpha_i^{-1} - \mathrm{Tan}\alpha^{-1})$$

If alignment is perfect, e = 0 and

$$\mathrm{Tan}\alpha_i \Big|_{\text{all } i} = \mathrm{Tan}\alpha$$

Alignment is a two step procedure. The factors A and B as computed in equations 1a and 1b determine the translation of the section. The angle α computed as in equation 2b determines the rotation necessary to complete the alignment of the section.

Program Align computes the translation and rotation factors in accordance with equations 1 and 2b. It permits alignment of sections interactively. Program Input (Chapter II) computes the center of mass of all contours as well as the area enclosed by the contour and its perimeter.

Alignment Operation Illustrated.

An illustration of the alignment operation is presented in fig.3.1 through fig.3.4. Fig.3.1 presents a display of the reference section (No. 32) with a Z-axis coordinate of 112 units. Contours marked 1,2 and 3 represent the sciatic nerve sections and may be used for alignment. Fig.3.2 displays the section (No. 35) being aligned to the reference section. Fig.3.3 shows this section translated with respect to the reference section. The translation factors are displayed in the upper left corner. Rotation is the next step in the alignment operation. Fig.3.4 displays section number 35 rotated with respect to the reference section. This completes the first iteration in the alignment operation. No improvement in alignment is seen after the third iteration of the alignment operation. Satisfactory alignment of two sections is achieved within three iterations.

3.4 Graphics Display.

The graphic display module of the Lung System permits the viewer to examine the reconstructed lung in three dimensions. It is possible to examine the lung from different angles of view by specifying the angle of rotation of the lung about X,Y or Z-axis. The 3-D picture may be previewed on-line on a storage tube terminal. Permanent

Fig. 3.1. Computer display of section number 32 (Z=112). Contours marked 1,2,3 are the sciatic nerve sections used for alignment purposes. Contour 4 represents the lung section. Contours 7 and 9 are the outlines of tumor nodule sections in this section.

SECTION NO 32 AT Z= 112

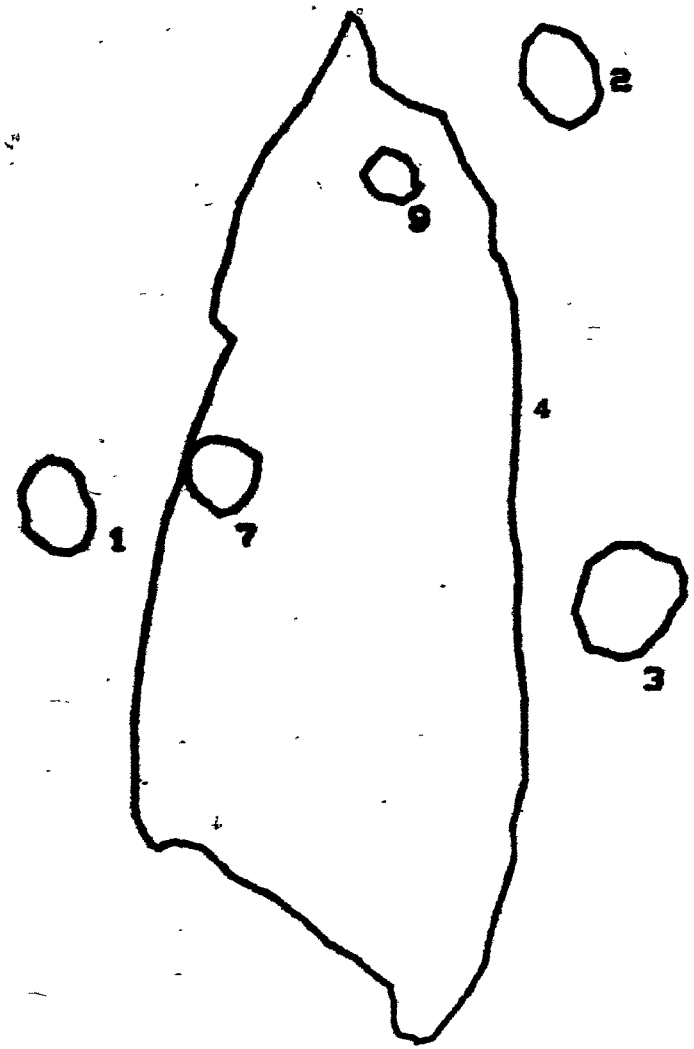

Fig. 3.2. Computer display of section number 35 (Z=71). Contours 1,2,3 are the sciatic nerve contours in this section. Contour 4 represents the lung section. Contours 5, 7 and 8 are the outlines of tumor nodule sections in section number 35.

SECTION NO 35 AT Z= 71

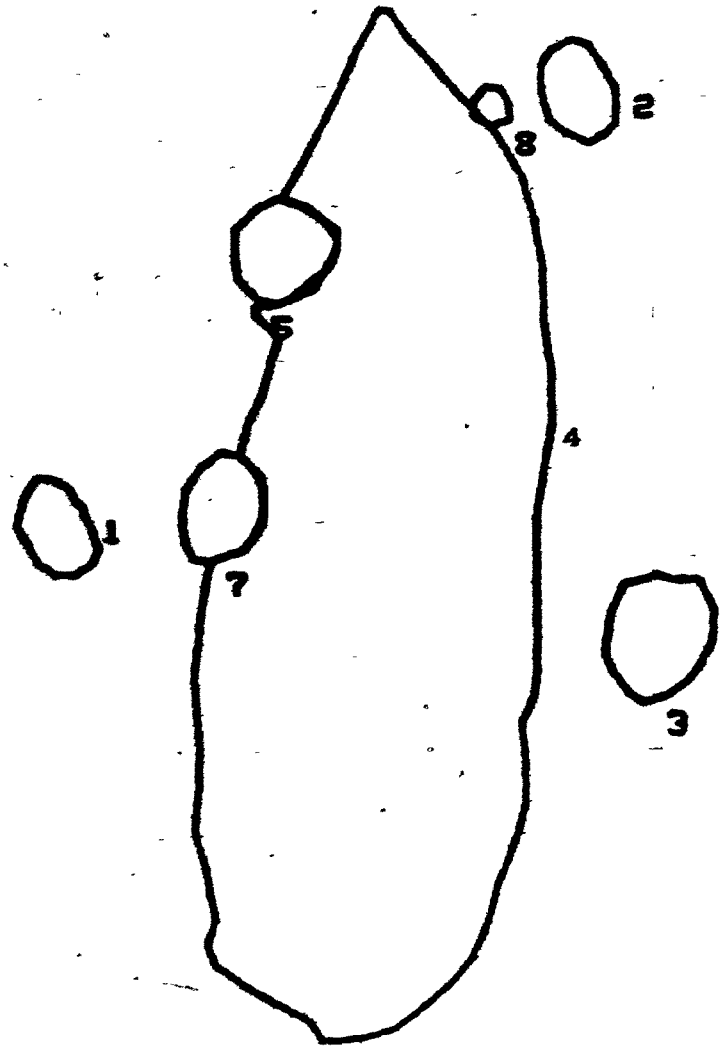

Fig. 3.3. Computer display of section number 35 translated (by factors indicated in upper left corner) to align it with section number 32. The translation factors are computed by applying a least squares error criteria to the position of contours 1, 2, 3 in the two sections being aligned.

TRANSLATED BY X= -3.00
Y= -2.67

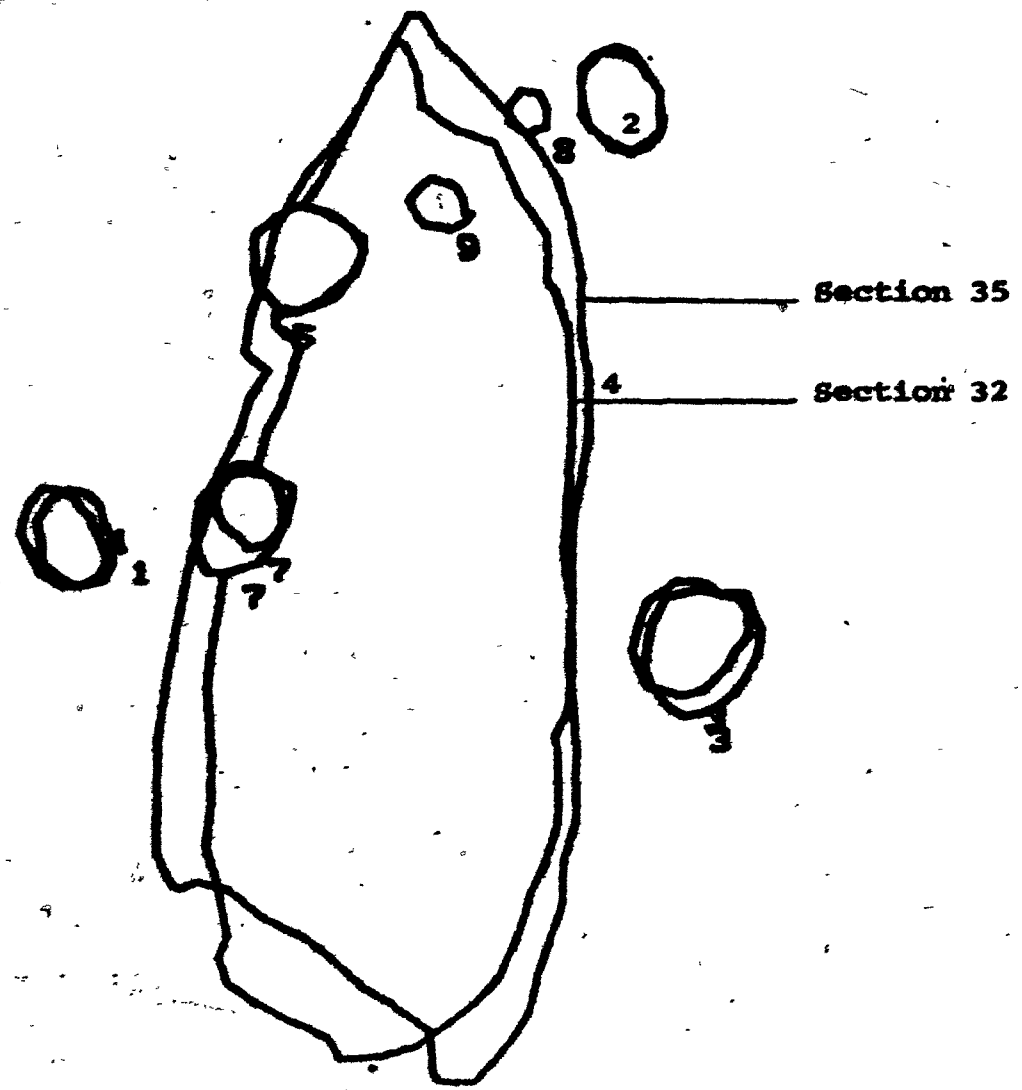

Fig. 3.4. Computer display of section number 35 rotated (by rotation angle indicated in upper left corner) to align it with section number 32. The rotation angle is computed by applying a least squares error criteria to the position of contours 1, 2, 3 in the two sections being aligned.

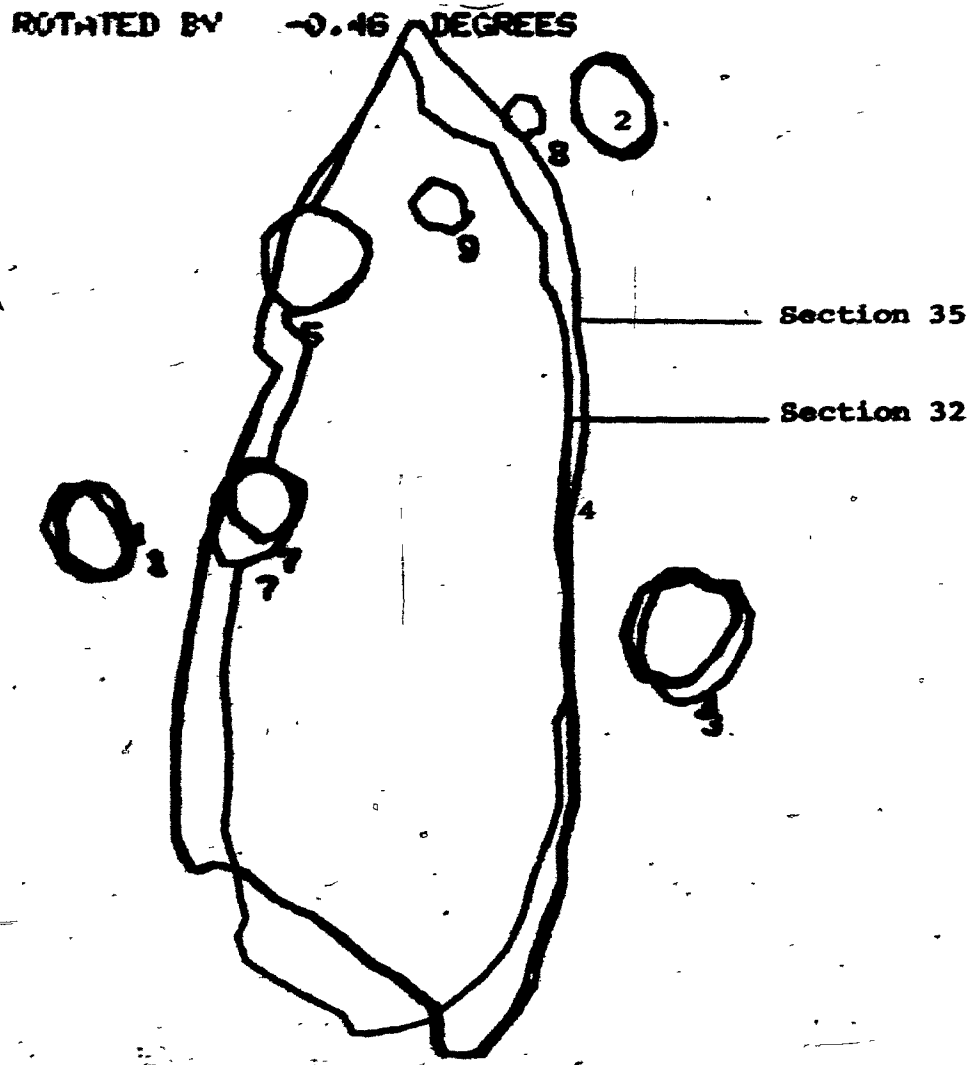
ROTATED BY -0.46 DEGREES
2
8
9
5
Section 35
Section 32
1
7
4
3

colored-copies of the picture are obtained by directing the output to the digital plotter.

The Stereo display system we developed results in a three dimensional wire-mesh model of the lung. The following section deals with the principles of stereo picture generation. The necessary transformations are also developed.

3.5 Principle Of Stereo Pictures.

Man's ability to perceive depth by fusing together the two images (one in each eye) of an object is the basis of stereo pictures. Essentially, a pair of perspective projections of the object on a common plane is obtained. The two pictures when viewed through a stereoscope (or even with unaided eyes with some practice) enable a 3-D perception of the object (17).

Central to the principle of stereo pictures is the generation of perspective projections of an object. A photograph of an object is essentially a projection of the object. If one imagines a picture plane to be interposed between the object and the eye (camera lens), then the locus of all points in the picture plane and on the pencil of rays emanating from the object and converging at the eye (camera lens) would define the perspective view of the object.

Principle of Perspective Projections.

This is illustrated in fig.3.5 and fig.3.6. The Projection of triangle ABC on a plane P is defined by A'B'C'. The projection is obtained by drawing rays through points A,B,C from the center O. The points A', B', C' in which the rays intersect the plane are the projections of points A, B, C, respectively. Fig.3.6 illustrates the projection of a straight line on an arbitrary plane. It is clear therefore, that the projection of a straight line is the locus of the projections of points on the line (36). Fig.3.7 serves to display a perspective view of a cube.

Mathematical Basis Of Perspective Projections.

Let the set of coordinates X_i, Y_i, Z_i describe the three dimensional object. Let the picture plane (the plane of projection) be defined by Z = 0, and let the object be behind this plane. The viewing point may be assumed to be at a, b, c.

The projection of the object onto the viewing plane will be defined by the set of points on the viewing plane X_i', Y_i' and $Z_i = 0$, where the line joining the points X_i, Y_i and Z_i to the viewing point a,b,c intersect the picture plane. Similar triangles can now be established as shown in

Fig. 3.5. The perspective projection of triangle ABC on a plane P is obtained by drawing a pencil of rays originating at the view point O, touching points A, B, C and intercepting the plane P at points A', B', C'.

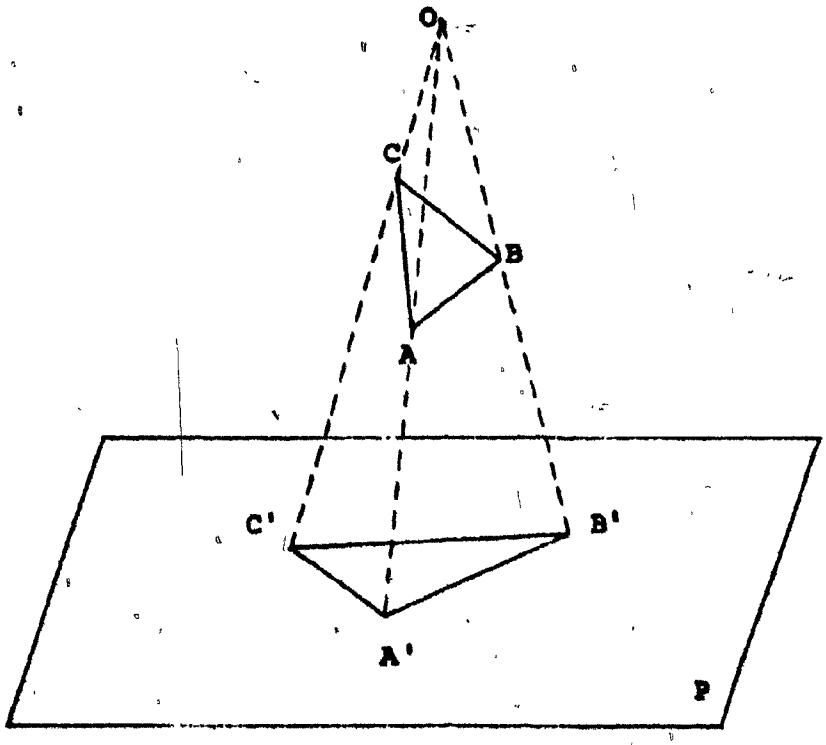

PERSPECTIVE PROJECTION OF TRIANGLE ABC ON A PLANE P

Fig. 3.6. The projection of the line ABCD on an arbitrary plane P is the locus of the projection of the points on the line.

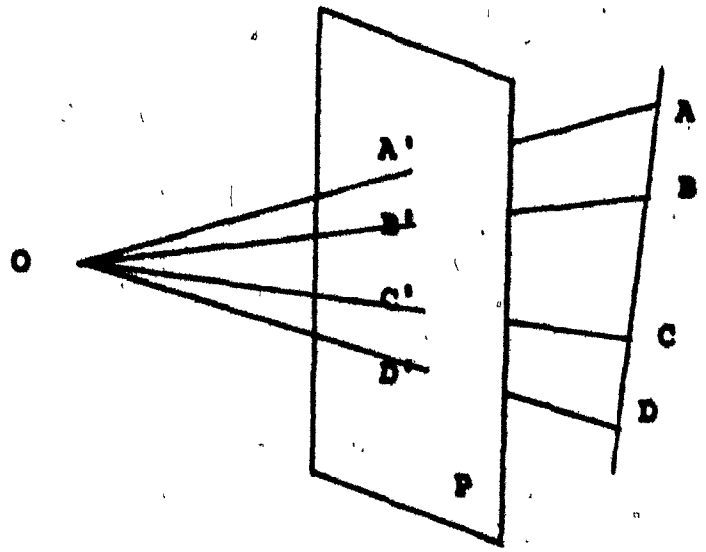

PROJECTION OF LINE AND OF AN ARBITRARY PLANE P

Fig. 3.7. Perspective view of a cube on a plane P illustrated.

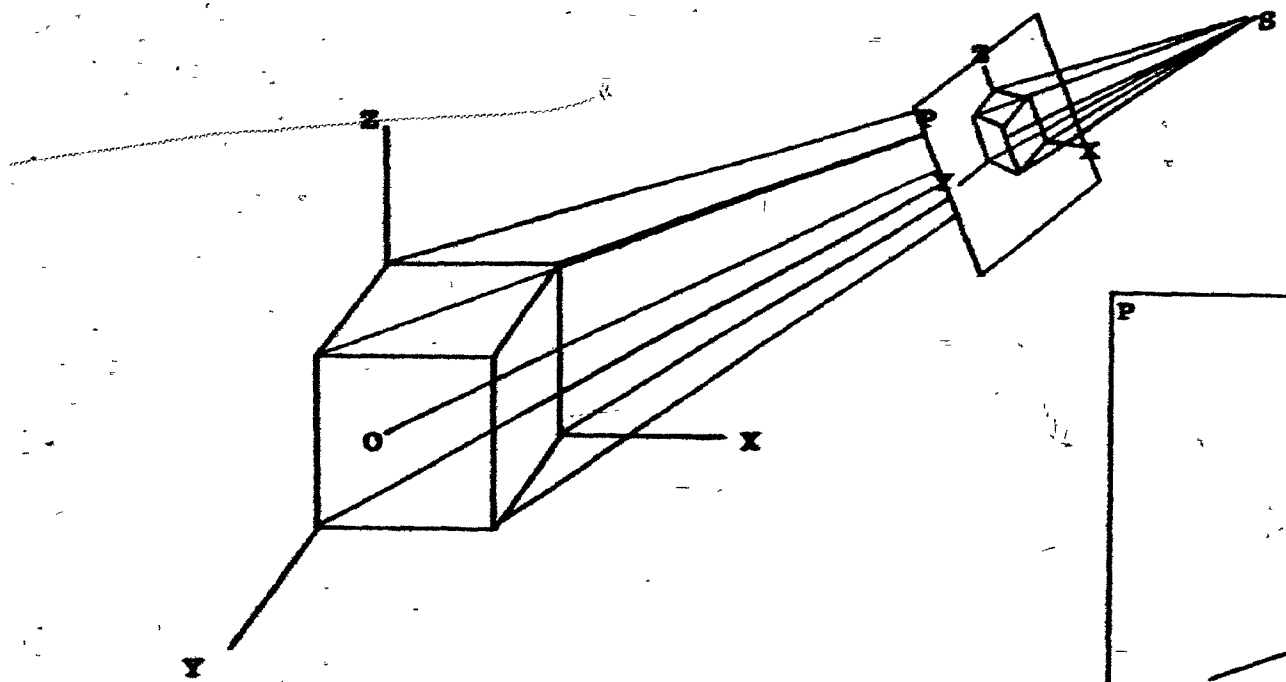

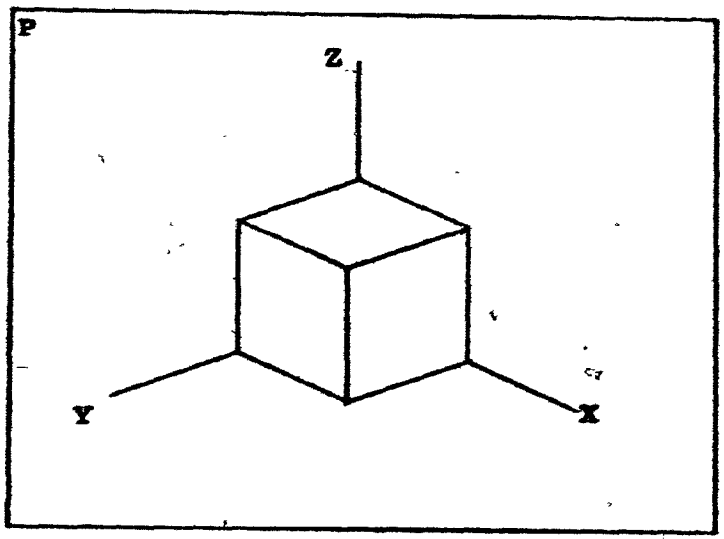

PERSPECTIVE VIEW OF A CUBE

fig.3.8 resulting in the following relationships.

$$\frac{X_1' - a}{X_1 - a} = \frac{Y_1' - b}{Y_1 - b} = \frac{-c}{Z_1 - c}$$

Therefore,

$$X_1' = (aZ_1 - cX_1)/(Z_1 - c)$$
$$Y_1' = (bZ_1 - cY_1)/(Z_1 - c)$$
$$Z_1' = 0$$

Homogeneous Coordinates.

If the coordinates of a point in three dimensions is written as a 4 vector ie. as (x y z d), where d can be a scale factor, then it is possible to carry out the operations of rotation, translation, perspective transformation and scaling by a single 4*4 transformation matrix 'T' (1).

$$\left[\begin{array}{c|c} 3*3 & \begin{matrix}3\\*\\1\end{matrix} \\ \hline 1*3 & 1*1 \end{array}\right] = T$$

The 3*3 matrix produces a linear transformation in the form of rotation. The 1*3 row matrix produces translation. The 3*1 column matrix produces perspective transformation and

Fig. 3.8. An illustration of the perspective projection of a point P_i on the viewing plane Z=0. The view point O is displayed at 'a' units on the X-axis. Due to similar triangles $\frac{X_i' - a}{X_i - a} = \frac{h}{z_i + h}$

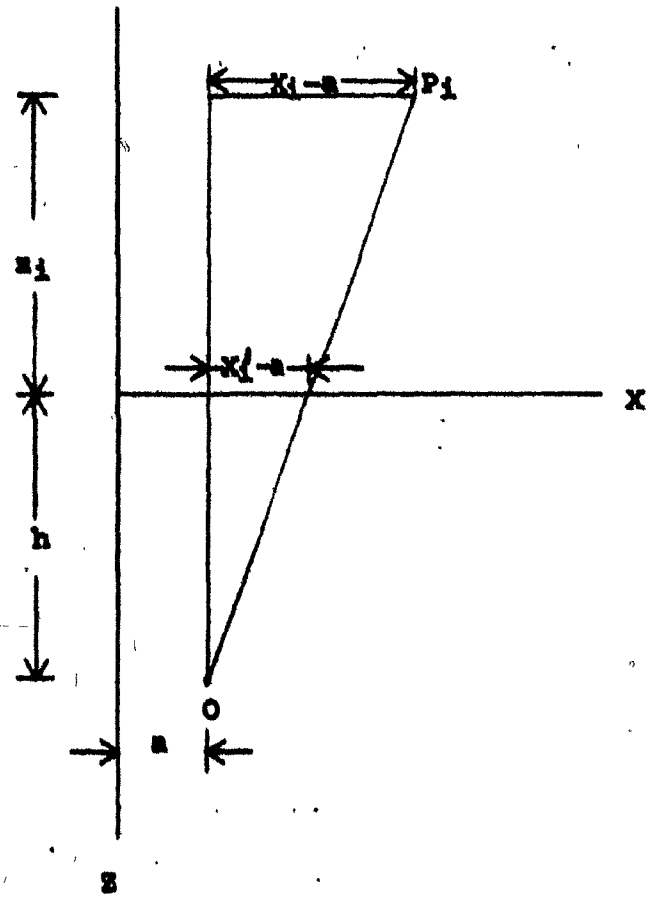

PERSPECTIVE PROJECTION OF POINT P_i ON THE PLANE Z=O

the 1#1 element can be used to produce overall scaling.

Mathematics Of Stereo Picture Generation.

In what follows, all the principles outlined above have been utilized to arrive at the formulation of matrix operators to eventually generate a stereo pair of the object in question. In keeping with the objective of being able to view the object from any desired viewpoint, the following outlines the method to translate, rotate about any desired axis and subsequently produce a pair of perspective pictures. The various matrices are multiplied in the order in which the transformations are performed.

The object is first centered ie. the origin of the coordinate system is moved to the center of the screen and coincident with the center of gravity of the object. The following matrix is used for this operation.

$$[\,X\ Y\ Z\ 1\,]\begin{bmatrix}1&0&0&0\\0&1&0&0\\0&0&1&0\\p&q&r&1\end{bmatrix} = [\,X'\ Y'\ Z'\ 1\,]$$

The factors p, q, r are established by first determining the center of gravity of the object and the center of the display screen. Rotation about the X, Y or Z- axis can be per-

formed by the following three matrices (2) respectively.

Rotation around the X-axis.

$$\begin{bmatrix} 1 & 0 & 0 & 0 \\ 0 & \cos\alpha & -\sin\alpha & 0 \\ 0 & \sin\alpha & \cos\alpha & 0 \\ 0 & 0 & 0 & 1 \end{bmatrix}$$

Rotation around the Y-axis.

$$\begin{bmatrix} \cos\alpha & 0 & \sin\alpha & 0 \\ 0 & 1 & 0 & 0 \\ -\sin\alpha & 0 & \cos\alpha & 0 \\ 0 & 0 & 0 & 1 \end{bmatrix}$$

Rotation around the Z-axis.

$$\begin{bmatrix} \cos\alpha & -\sin\alpha & 0 & 0 \\ \sin\alpha & \cos\alpha & 0 & 0 \\ 0 & 0 & 1 & 0 \\ e & f & g & h \end{bmatrix}$$

where e, f, g are the translation factors and d is the scale factor. The translation at this stage serves to move the object behind the screen so that the perspective view does not get distorted.

The perspective transformation for each eye is obtained

by considering the view points at a distance 'h' in front of the picture plane and symmetrically placed about the Z-axis on a line Y = 0 ie, if the eye separation is 2e, the viewing points are -e, 0, -h for the left eye and e, 0, -h for the right eye.

Therefore,

$$X_i' \text{ left} = (hX_i - eZ_i)/(Z_i + h)$$
$$X_i' \text{ right} = (hX_i + eZ_i)/(Z_i + h)$$
$$Y_i' \text{ left} = hY_i/(Z_i + h)$$
$$= Y_i' \text{ right}$$

Since h is large compared to Z_i,

$$X_i' \text{ left} = X_i - Z_i(e/h)$$
$$X_i' \text{ right} = X_i + Z_i(e/h)$$

The matrices for the left and the right eye are therefore:

For the left eye:

$$\begin{bmatrix} 1 & 0 & 0 & 0 \\ 0 & 1 & 0 & 0 \\ -e/h & 0 & 0 & 0 \\ m & 0 & 0 & 1 \end{bmatrix}$$

For the right eye:

$$\begin{bmatrix} 1 & 0 & 0 & 0 \\ 0 & 1 & 0 & 0 \\ e/h & 0 & 0 & 0 \\ n & 0 & 0 & 1 \end{bmatrix}$$

Where e and n are the translation factors to create the proper separation between the two views.

In conclusion, if the composite matrix (the matrix obtained by multiplying the proper matrices) is 'A' and if the coordinates X_i , Y_i and Z_i of the object are written in the matrix form as [X Y Z 1] then the matrix [X' Y' Z' 1] would yield the transformed coordinates.Where,

$$[\ X'\ Y'\ Z'\ 1\ ] = [\ X\ Y\ Z\ 1\ ] * [\ A\ ]$$

Program Stereo Picture formulates the translation, rotation and perspective transformation matrices. The composite matrix obtained by multiplying the required transformation matrices is used by Program Picture to display a stereo pair of the lung.

Samples of stereo pictures produced by the stereo display system are presented in fig.3.9 through fig.3.13. These pictures were obtained with the following picture par-

Fig. 3.9. Stereoscopic display of a reconstructed lung.

Scale. 1:8.3

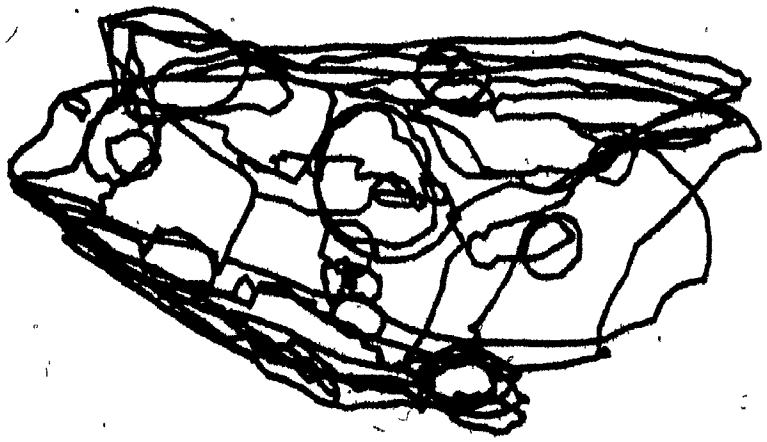

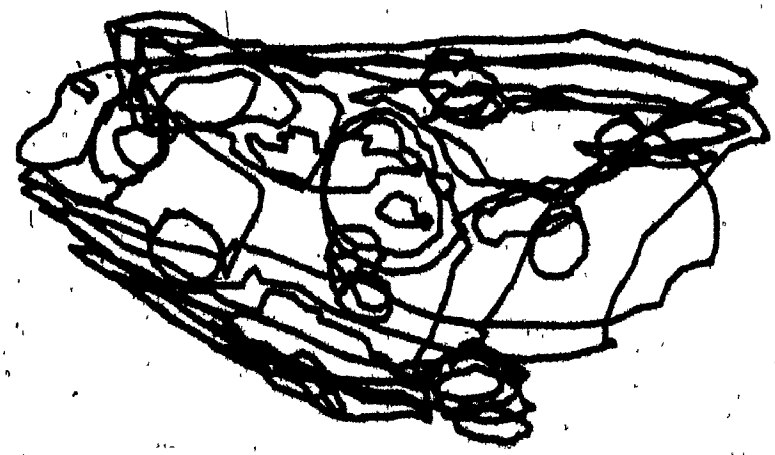

Fig. 3.10. Stereoscopic color display of a reconstructed lung. Scale. 1:8.3

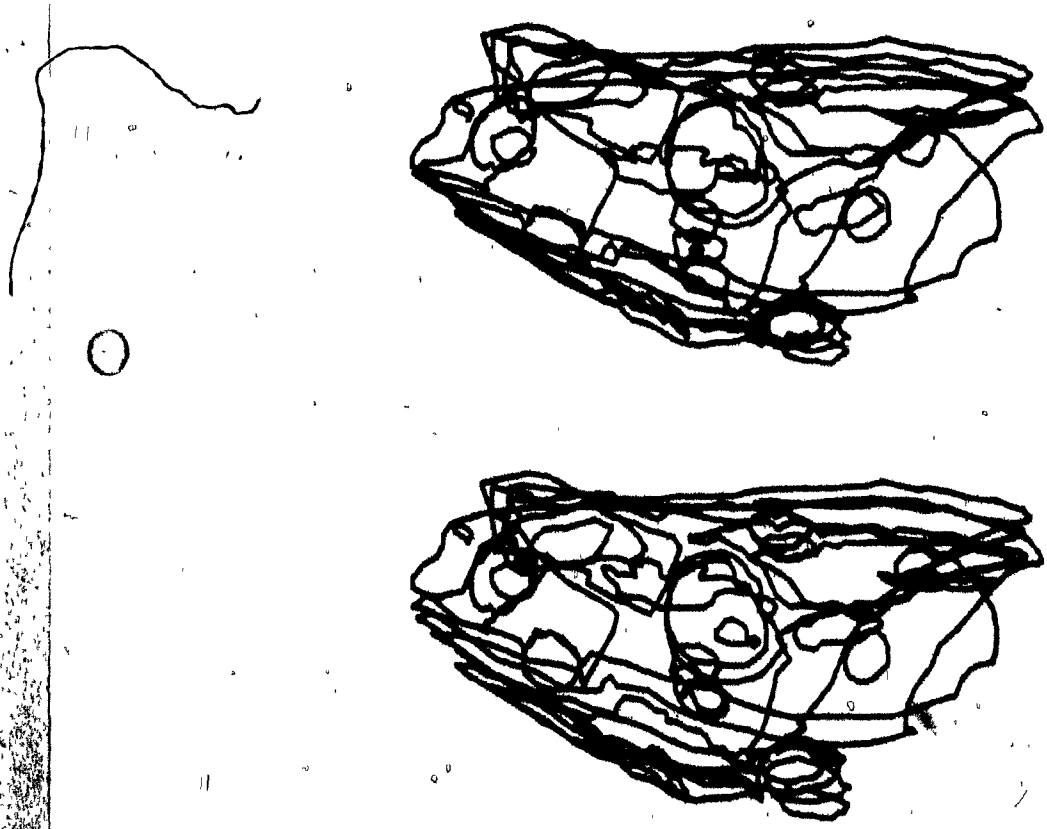

ameters.

a.	The angles of rotation around X, Y, Z axes	30
b.	The picture scale factor	0.5
c.	The eye separation distance	50 mm.
d.	The viewing distance	50 cm.
e.	The separation between the pictures	20 cm.

Fig.3.9 displays the stereo pair of the lung. The same picture is visualized with greater clarity in fig.3.10 wherein the lung and tumor nodule contours are drawn in two different colors. Fig.3.11-fig.3.13 display the lung as viewed from different angles of view.

3.6 Quantitative Data Extraction.

With programs developed to-date we can extract the volume , surface area and the sphericity index of the tumor nodules. The volume and surface area can be estimated to within 5% (test results included in appendix A). The inter-nodule distance matrix is also available for each lung.

The volume of a tumor nodule is computed by adding up the volumes enclosed between every pair of the planar sections. The volume (V) between any pair of planar sections with cross-sectional areas A1 and A2 , and separation T is:

Fig. 3.11. Stereoscopic display of a reconstructed lung rotated 30 degrees around the horizontal axis. Scale. 1:0.3

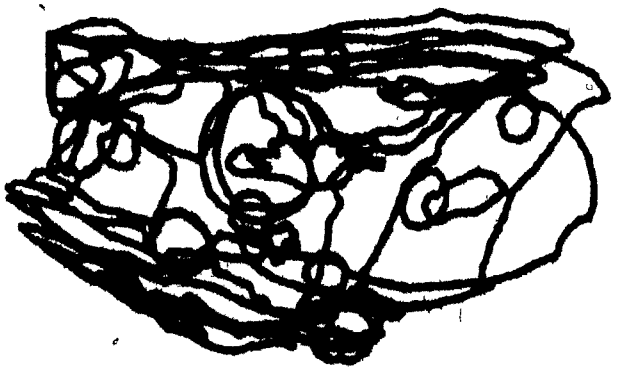

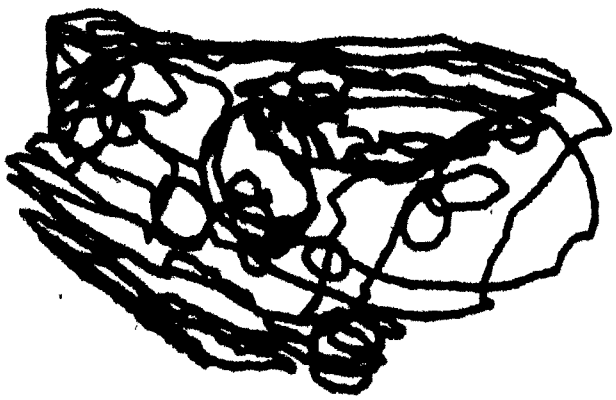

Fig. 3.12. Stereoscopic display of a reconstructed lung rotated 30 degrees around the vertical axis. Scale. 1:8.3

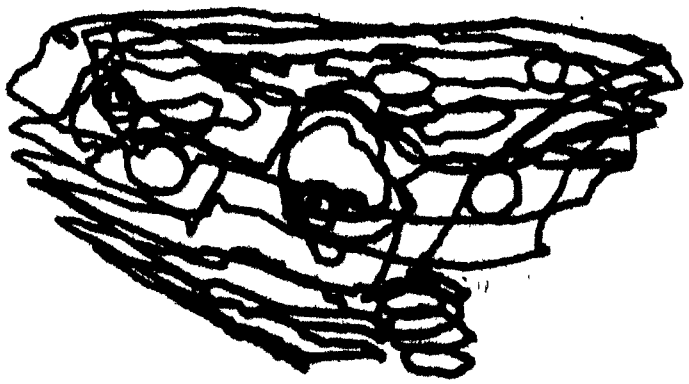

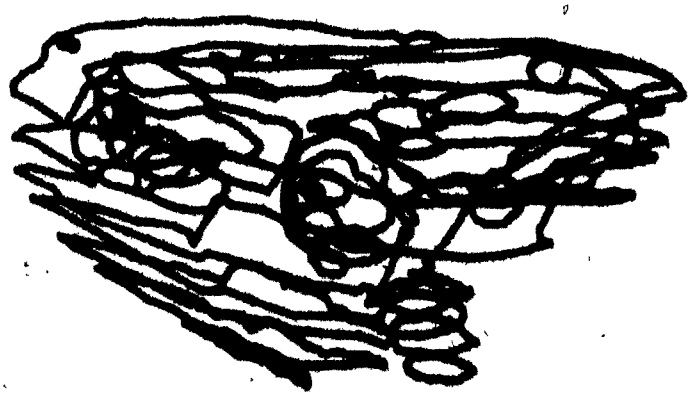

Fig. 3.13. Stereoscopic display of a reconstructed lung rotated 30 degrees around the axis normal to the plane of the paper. Scale. 1:8.3

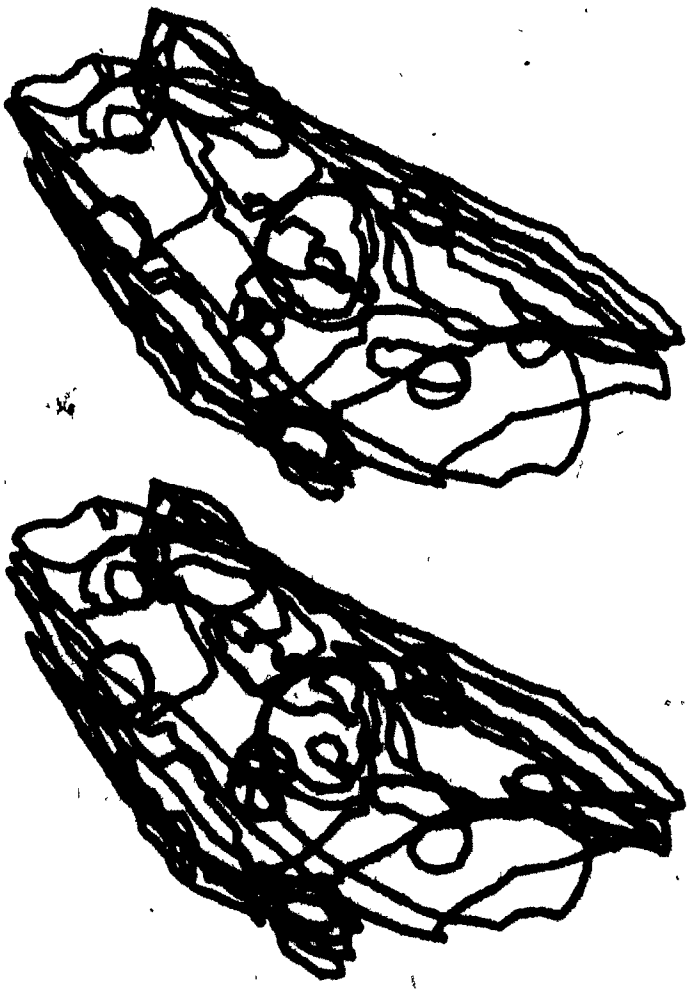

$$V = (A1 + A2)*T/2$$

Like the computation of the volume, the total surface area of a tumor nodule is computed by adding up the surface area between every pair of adjoining contours. The surface between two adjoining contours is approximated by triangular tiles as shown in fig.3.14a and fig.3.14b. The edges of the triangular tiles are 'determined' by an algorithm that connects the diagonals between points on the two contours. The algorithm first connects the two closest points (a-b) on the two contours, then connects a to c if distance ac is shorter than (or equal to) bd or else connects b to d. This operation is illustrated in fig.3.14b. The entire surface is 'triangulated' and its surface area determined.

The sphericity index (S.I.) of a tumor nodule is determined by the following relation:

$$S.I. = 1\sqrt{V}/2\sqrt{A}$$

where V is the volume and A is the surface area of the tumor nodule. The sphericity index attains a maximum value for a sphere (S.I.=.46).

Program Data extracts the required quantitative data. Included in this module are Program Direction, Program Triangulation, Program Trngt, and Program Collate.

Fig. 3.14a. The surface between two corresponding contours X and Y in adjoining sections can be approximated by constructing triangular tiles as indicated in Fig. 3.14b.

Fig. 3.14b. The two closest points (a,b) on the two contours X and Y are connected first. Next point a is connected to c if the distance ac is less than or equal to distance bd (resulting in triangle abc) or else point b is connected to point d (resulting in triangle abd). The entire surface is 'triangulated' on the basis of this rule.

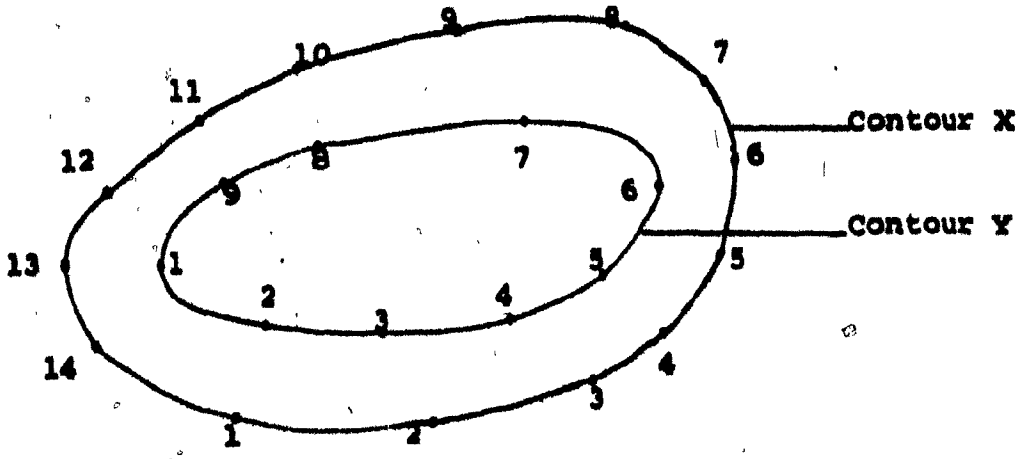

Fig. 3.14a

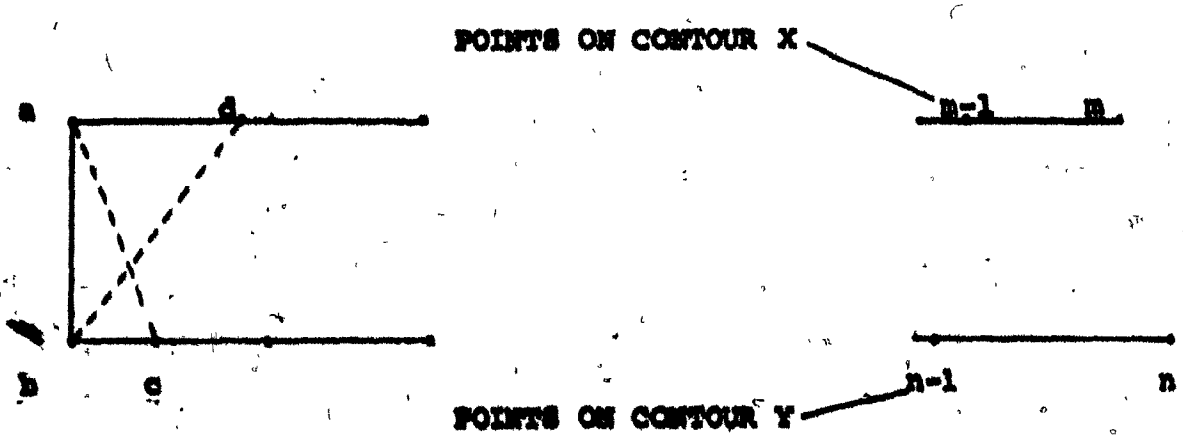

Fig. 3.14b

3.7 System Performance Measurements.

The performance of a software system may be assessed by the measurement of the following parameters.

1. I/O (Input/Output) count: This is the number of QIO's issued on behalf of the program. The I/O count is a measure of the utilization of the executive I/O related modules.
2. CPU Time: This is the amount of central processing unit time required by the program to complete execution. The CPU time is a direct measure of the CPU usage.
3. Memory Demand: This is the amount of memory required (in kilo words) times the CPU time (in ticks=1/60 second) required by the program to execute.

The above parameters were measured for the data acquisition programs, picture generation programs and the quantitative analysis programs. In addition, the cost is also computed based on the prevailing rates of computer services at the Biomedical Eng. Unit, McGill University. The terminal connect time (which contributes to the cost) is recorded as well.

Parameters Relating To the Data Acquisition Programs.

A single section of the mouse lung was digitized and aligned (with respect to a reference section). The following performance parameters were recorded.

1. Terminal Connect Time: 14min.
2. I/O Count: 1622
3. CPU Time: 17 sec. and 40 ticks
4. Memory Demand: 1049*1000 kw*ticks
5. Cost per section: 2.0 dollars (approximately)

Based on the above estimate, the cost of digitizing 60 sections in a lung would be approximately 120.0 dollars.

Parameters Relating To 3-D Stereoscopic Color Display Of A Lung.

1. Terminal Connect Time: 7 min.
2. I/O Count: 882
3. CPU Time: 21 sec. and 51 ticks.
4. Memory Demand: 291*1000 kw*ticks
5. Cost per picture: 65 cents (approximately)

Parameters Relating To The Quantitative Analysis Programs.

1. Terminal Connect Time: 1 min
2. I/O Count: 377

3. CPU Time: 24 sec. and 12 ticks.

4. Memory Demand: 79*1000 kw*ticks

5. Cost per Lung: 60 cents (approximately)

CHAPTER IV

EXPERIMENTS TO STUDY METASTATIC GROWTH

4.1 Introduction.

In this Chapter I describe experiments conducted to study the growth of tumor nodules in mouse lung. The three dimensional spatial distribution of tumor nodules in the upper left lobe of the lung is also investigated. A hypothesis concerning the growth of metastatic tumor nodules in mouse lung is postulated.

4.2 Rationale.

Metastases occur following the release of cells from a primary tumor (42). The blood-borne metastases go through a series of stages (3,7,42,47), viz. cell separation, dissemination, initial establishment and proliferation, eventually leading to 'clinical' metastases. Once the cancer emboli are arrested in a capillary bed they must penetrate the vascular endothelium to establish metastatic foci. Subsequent growth of tumor nodules requires the development of an adequate vascular supply (16,42,46). Factors effecting the proliferation of tumor cells can be grouped under nutrition, growth stimulating factors, and growth inhibitory factors (38). The nature of growth of tumors at this stage is dependent on the mutual interactions of these factors (Seed and Soil hypothesis, Paget 1889). The role of these factors on the growth of tumors is poorly understood (7,9,32).

The point of our experiments was to systematically analyse the three dimensional spatial distribution of the tumor nodules in mouse lung (upper left lobe) and in this way determine the effect of microenvironment on growth.

4.3 Materials And Methods.

Thirty C57BL/6J mice were inoculated with 2x10^5 B16

mouse melanoma cells (34). One group of fifteen mice was sacrificed after 19 days and the remaining fifteen were sacrificed after 28 days. The left upper lobe of the mice lung (hitherto referred as the 'lung') of six animals, three from each group were prepared for histological sectioning in accordance with standard procedures. The lung tissue was fixed in 10% formal saline and embedded in paraffin wax. Prior to the sectioning, three pieces of sciatic nerve were introduced into the paraffin wax block approximately perpendicular to the plane of sectioning (these later served as alignment guides during the serial reconstruction). The lung was serially sectioned on an American Optical Corporation "820" Spencer microtome, into sections 8 microns thick. During sectioning ,the temperature of the paraffin block was kept approximately constant by repeatedly freezing it for about 2-3 minutes. The serial sections were stained and mounted on microscopic slides.

The Interactive Computer System (Lung System, Chapter II and III) enables digitization of the lung sections on the microscopic slides. Using this system the entire lung can be reconstructed and relevant quantitative data (such as volume, surface area, sphericity index of tumor nodules) can be computed.

The histological procedures are subject to systematic

shrinkage and compression errors. Experiments were conducted to quantitate these serial sectioning artifacts (appendix B). All data are corrected for these systematic histological errors.

1. Data Acquisition.

The slide to be digitized is mounted on the projector and the image of the contours which is projected (magnified to 27.36X) on the "tablet", can be digitized by moving the 'pen' along the contour. Under program control, the position of points along the contour are transmitted to the computer and displayed on a CRT. The 'digital' description of the contour (in terms of the x, y coordinates of the points along the contour) is assimilated into the data base on the storage disc. A typical section is shown in fig.4.1, wherein contours 1,2 and 3 are the contours of the sciatic nerves, contour 4 is the contour of the lung and contours 9-12 are the contours of the tumor nodules. Each contour may consist of a maximum of 127 coordinate points. A maximum of 64 different sections can be digitized for each lung.

2. Alignment Of Sections.

The alignment of a section (with respect to another section) is achieved by bringing the center of the corres-

Fig. 4.1. Computer display of a typical lung section digitised from its histological slide (magnified 27.36X). Contours marked 1, 2, 3 are the sciatic nerve contours used as alignment guides. Contour marked 4 represents the lung section and contours marked 9, 10, 11, 12 represent tumor nodule contours. Scale. 1:14.1

SECT.NO.= 27 Z= 161
WANT TO ALIGN SECTION 27?(Y/N)

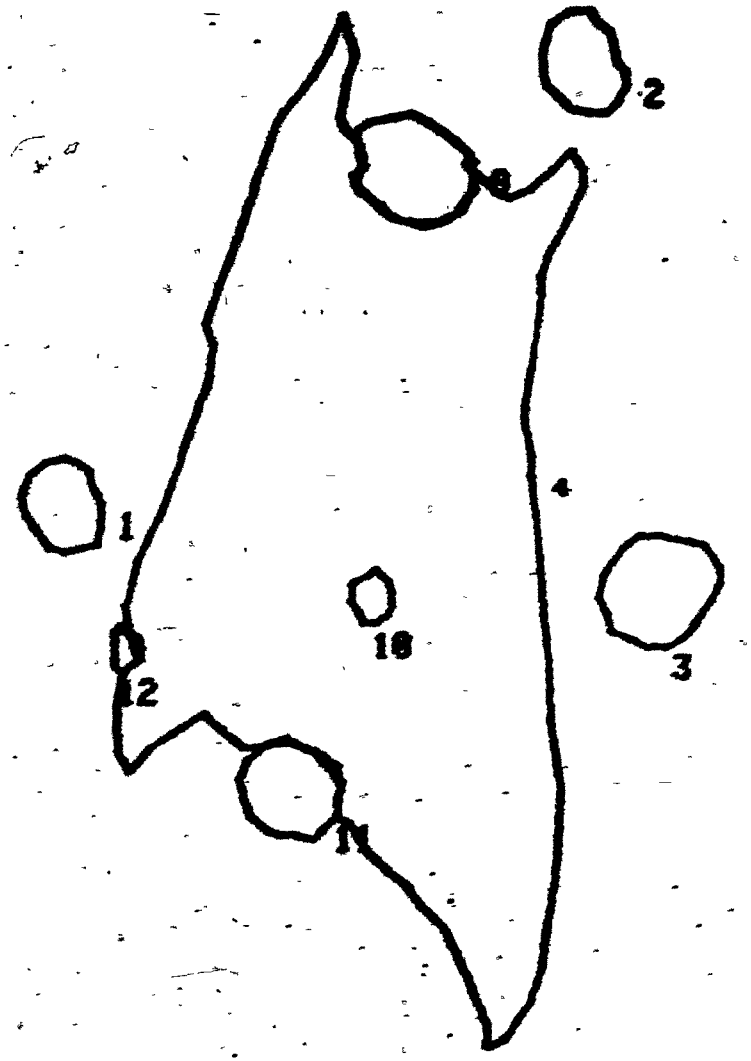

ponding sciatic nerve contours into close correspondence with each other using a least squared error criteria (Chapter III).

The data base resulting after the completion of the data acquisition and alignment procedures for any lung can be directly used by the display and analysis programs.

3. Three Dimensional Display Of The Lung.

The lung reconstructed from serial sections is displayed as a stereo pair. The Lung System permits views to be obtained from different angles of view. This display facilitates the observation of the spatial relationships of the tumor nodules.

4. Quantitative Analysis Of The Reconstructed Lung.

Programs have been developed to compute, for each lung, the volume, surface area, the sphericity index and the center-to-center distance of tumor nodules.

5. Monte Carlo Simulations Of Three Dimensional Growth Patterns In The Lung.

Is the spatial distribution of tumor nodules in the

lung random ? To determine the characteristics of a random spatial distribution the following simulation (called a Monte Carlo simulation) was performed. For each lung under study, random points were generated. In each lung as many points as the number of tumor nodules incident in the experimental lung were generated. The center-to-center distance of the randomly generated tumor nodule positions were computed. By repeating the trials with different seed values of the random number generator, adequate data on the first neighbor distances can be collected to determine the distribution of the first neighbor distances of randomly generated points in any lung.

The distribution of the first neighbor distances of random points in three dimensional space is also known. If r represents the first neighbor distance, then the probability density function (of the nearest neighbor distance) f(r) is given (18),

$$f(r) = 4\pi r^2 \exp(-\tfrac{4}{3}\rho\pi r^3)dr$$

where ρ is the number density of points.
The mean nearest neighbor distance R is

$$R = (\tfrac{1}{\rho})^{1/2}/(4\pi/3)^{1/3}$$

and the variance V is

$$V = (\tfrac{1}{\rho})^{1/2}/(4\pi/3)^{2/3} - (\tfrac{4}{3})^2/(\tfrac{4}{3}\rho\pi)^{1/3}$$

4.4 Results.

In Tables B the data computed for each lung under study are displayed. Each Table details the volume, diameter of an equivalent spheroid, surface area and sphericity index of each tumor in the lung. The association of the tumor nodule with bronchi or blood vessels is detailed. The peripheral or parenchymal nature of the tumors is also recorded. The corresponding stereograms for these lungs are found in fig.4.2-fig.4.7.

Table C summarizes the mean volume, mean surface area and the mean diameter of the tumor nodules. Group I lungs were obtained from mice sacrificed after 19 days and Group II mice were obtained from mice sacrificed after 38 days. The number of peripheral tumor nodules is larger than the number of parenchymal tumor nodules in both Group I and Group II lungs.

The average volume of peripheral tumors (.41 ml in Group I and 3.95 ml in Group II) is far greater compared to the average volume of the parenchymal tumors in both Group I (.06 ml) and Group II (.03 ml). The average volume of peripheral tumors in Group II (3.95 ml) is considerably greater compared to that in Group I (.41 ml). The average volume of parenchymal tumors (.03 ml) in Group II is the smallest of

Table 3(1). Summary of data concerning Lung 2A.

PR stands for peripheral, PC for parenchymal, PB for peribronchial and PV for perivascular tumor nodules.

TABLE B(1)

LUNG 2A

TUMOR NO.	VOLUME mm^3	DIAMETER mm	SURFACE AREA mm^2	SPHERICITY INDEX	PR or PC	PB	PV	NECROTIC	ANATOMICAL INFLUENCE
1	0.04	0.42	0.70	0.40	PR	PB	-	-	Chestwall & Diaphragm
2	0.08	0.53	1.40	0.36	PC	PB	-	-	-
3	0.04	0.42	1.31	0.31	PC	PB	PV	-	Bronchi
4	0.01	0.27	0.75	0.25	PR	-	-	-	-
5	0.06	0.48	1.64	0.31	PC	PB	PV	-	Blood vessels
6	0.03	0.38	0.74	0.36	PC	PB	PV	-	Blood vessels
7	0.06	0.48	1.44	0.33	PR	-	PV	-	Hilus & Blood vessels
8	0.06	0.48	1.03	0.38	PR	-	-	-	Chestwall
9	0.09	0.55	1.19	0.41	PC	PB	-	-	-

Table 3(2). Summary of data concerning Lung 6A.

PR stands for peripheral, PC for parenchymal, PB for peribronchial and PV for perivascular tumor nodules.

TABLE B(2)

LUNG 6A

TUMOR NO.	VOLUME mm^3	DIAMETER mm	SURFACE AREA mm^2	SPHERICITY INDEX	PR or PC	PB	PV	NECROTIC	ANATOMICAL INFLUENCE
1	0.25	0.78	3.17	0.35	PR	PB	PV	-	Chestwall & Bronchi
2	0.09	0.55	1.67	0.35	PR	-	-	-	-
3	0.30	0.82	2.61	0.42	PR & PC	-	-	-	Chestwall

Table B(3). Summary of data concerning Lung 10A. PR stands for peripheral, PC for parenchymal, PB for peribronchial and PV for perivascular tumor nodules.

TABLE B(3)

LUNG 10A

TUMOR NO.	VOLUME mm^3	DIAMETER mm	SURFACE AREA mm^2	SPHERICITY INDEX	PR or PC	PB	PV	NECROTIC	ANATOMICAL INFLUENCE
1	0.54	1.10	3.78	0.42	PR & PC	-	PV	-	Chestwall
2	0.14	0.64	1.55	0.42	PR & PC	-	PV	-	Chestwall
3	0.54	1.10	3.88	0.41	PR & PC	PB	PV	-	Chestwall
4	0.03	0.38	0.58	0.42	PR & PC	-	PV	-	Blood vessels
5	0.87	1.18	5.86	0.40	PR & PC	-	PV	-	Chestwall
6	0.12	0.61	1.38	0.42	PR & PC	PB	PV	-	-
7	0.40	0.91	3.05	0.42	PR & PC	-	PV	-	Chestwall & Blood vessels
8	0.99	1.24	8.18	0.35	PR	PB	PV	-	Chestwall & Diaphragm
9	0.23	0.76	2.83	0.36	PR & PC	-	-	-	-
10	0.29	0.82	4.12	0.33	PR	PB	PV	-	Chestwall
11	2.34	1.64	19.07	0.30	PR	-	-	necrotic	Mediasternum

Table B(4). Summary of data concerning Lung 15A.

PR stands for peripheral, PC for parenchymal, PB for peribronchial and PV for perivascular tumor nodules.

TABLE B(4)

LUNG 15A

TUMOR NO.	VOLUME mm^3	DIAMETER mm	SURFACE AREA mm^2	SPHERICITY INDEX	PR or PC	PB	PV	NECROTIC	ANATOMICAL INFLUENCE
1	7.23	2.40	35.57	0.32	PR	PB	PV	-	Chestwall
2	5.15	2.14	26.65	0.33	PR	-	PV	-	-
3	8.96	2.58	40.76	0.32	PR	PB	PV	-	-
4	0.02	0.33	0.55	0.34	PR & PC	-	PV	-	-

Table B(5). Summary of data concerning Lung 24A. PR stands for peripheral, PC for parenchymal, PB for peribronchial and PV for perivascular tumor nodules.

TABLE B(5)

LUNG 24A

TUMOR NO.	VOLUME mm^3	DIAMETER mm	SURFACE AREA mm^2	SPHERICITY INDEX	PR or PC	PB	PV	NECROTIC	ANATOMICAL INFLUENCE
1	22.01	3.48	134.93	0.24	PR	PB	PV	necrotic	-
2	0.21	0.73	4.39	0.29	PR	PB	-	-	-
3	0.05	0.46	1.16	0.35	PC	PB	PV	-	-
4	1.81	1.51	10.53	0.37	PR & PC	PB	PV	-	Blood vessels & Bronchi
5	0.01	0.27	0.57	0.30	PR	PB	-	-	-

Table B(6). Summary of data concerning Lung 26A. PR stands for peripheral, PC for parenchymal, PB for peribronchial, and PV for perivascular tumor nodules.

TABLE B(6)

LUNG 26A

TUMOR NO.	VOLUME mm^3	DIAMETER mm	SURFACE AREA mm^2	SPHERICITY INDEX	PR or PC	PB	PV	NECROTIC	ANATOMICAL INFLUENCE
1	6.16	2.28	30.38	0.33	PR & PC	PB	PV	-	Chestwall & Blood vessels
2	0.01	0.27	0.30	0.39	PC	-	-	-	-
3	3.53	1.89	22.26	0.32	PR & PC	PB	PV	-	Chestwall & Blood vessels
4	0.67	1.09	5.36	0.38	PR & PC	PB	PV	-	Blood vessels
5	2.33	1.66	19.20	0.30	PR	-	PV	-	Chestwall
6	0.83	1.16	6.65	0.36	PR & PC	PB	PV	-	Chestwall
7	0.27	0.80	3.80	0.33	PR	-	PV	-	Chestwall
8	0.04	0.42	1.43	0.30	PR	-	-	-	-

Fig. 4.2. A stereoscopic color display of lung 2A reconstructed. Blue contours pertain to the lung. Red contours indicate tumor nodules. Scale. 1:8.3

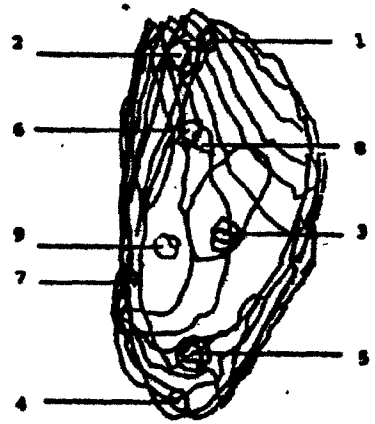

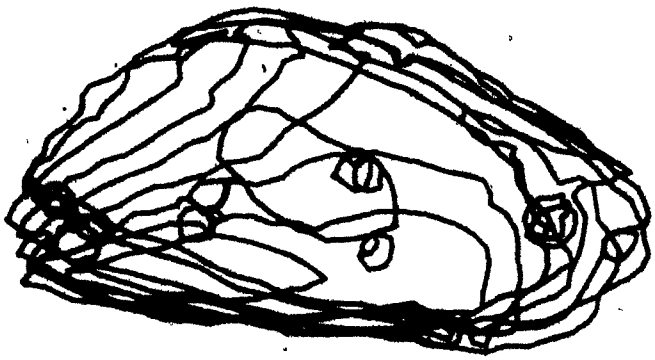

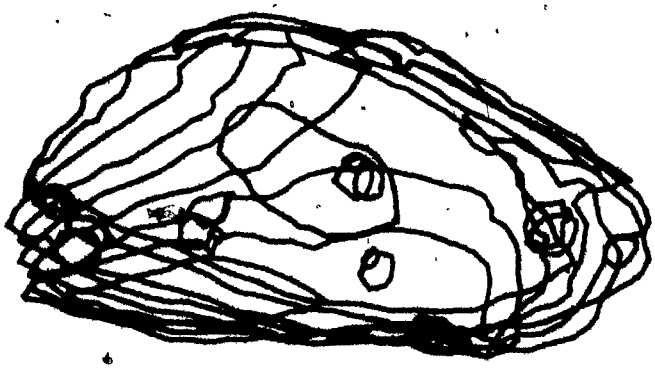

Fig. 4.3. A stereoscopic color display of lung 6A reconstructed. Blue contours pertain to the lung. Red contours indicate tumor nodules. Scale. 1:8.3

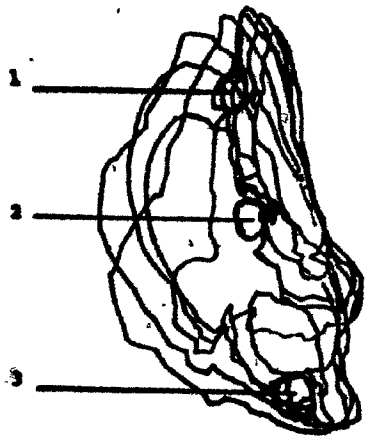

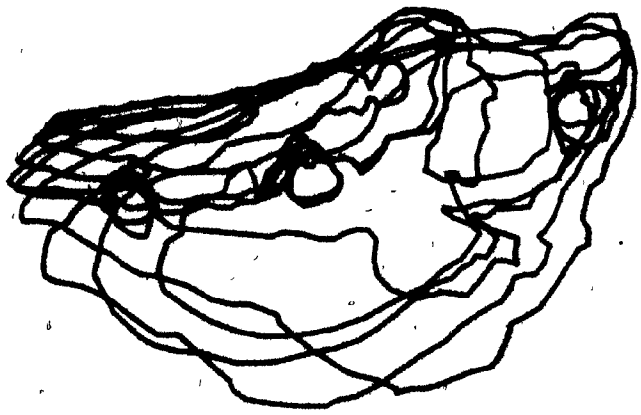

Fig. 4.4. A stereoscopic color display of lung 10A reconstructed. Blue contours pertain to the lung. Red contours indicate tumor nodules. Scale. 1:8.3

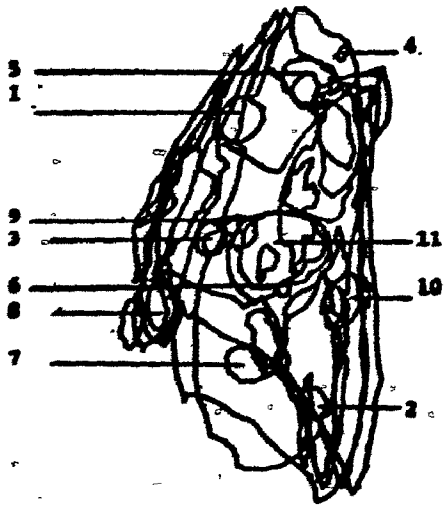

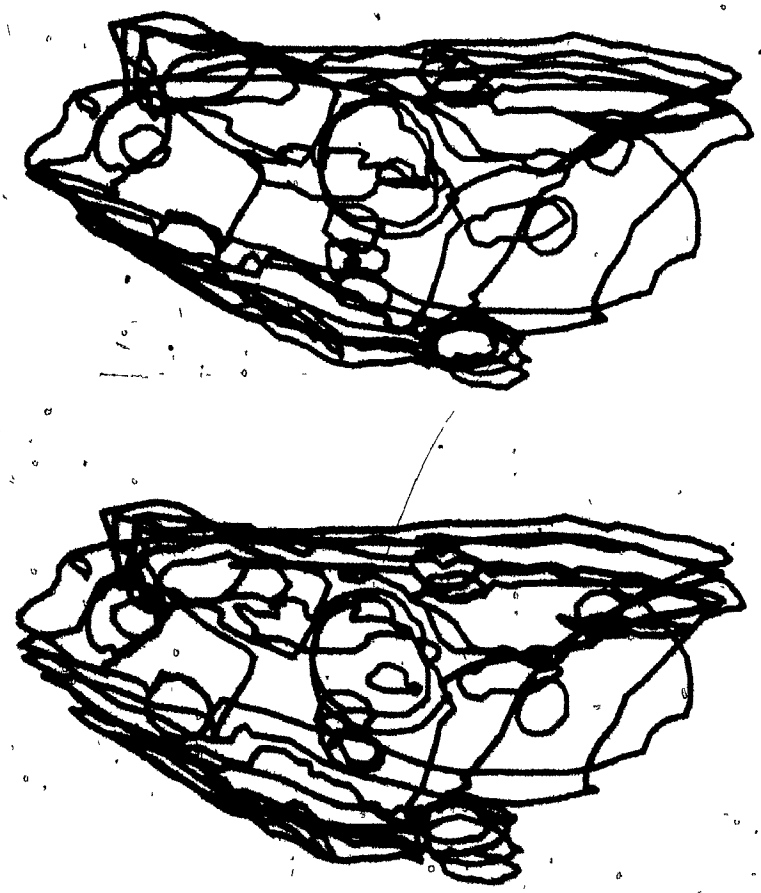

Fig. 4.5. A stereoscopic color display of lung 15A reconstructed. Blue contours pertain to the lung. Red contours indicate tumor nodules. Scale. 1:8.3

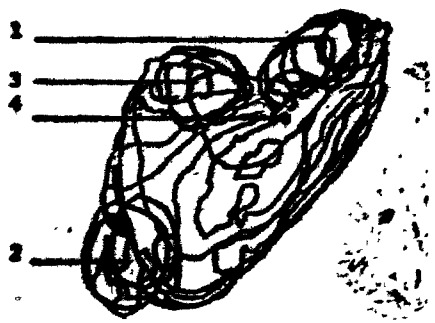

Fig. 4.6. A stereoscopic color display of lung 24A reconstructed. Blue contours pertain to the lung. Red contours indicate tumor nodules. Scale. 1:8.3

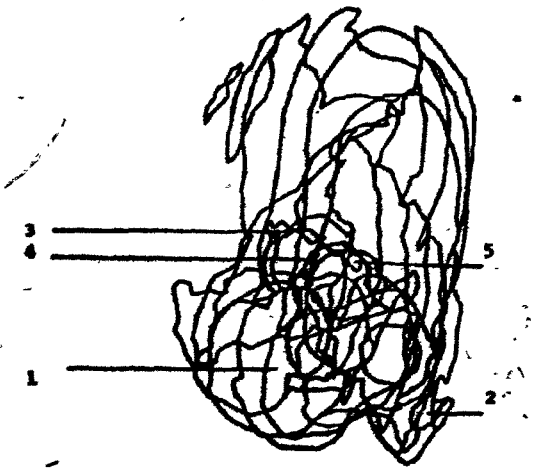

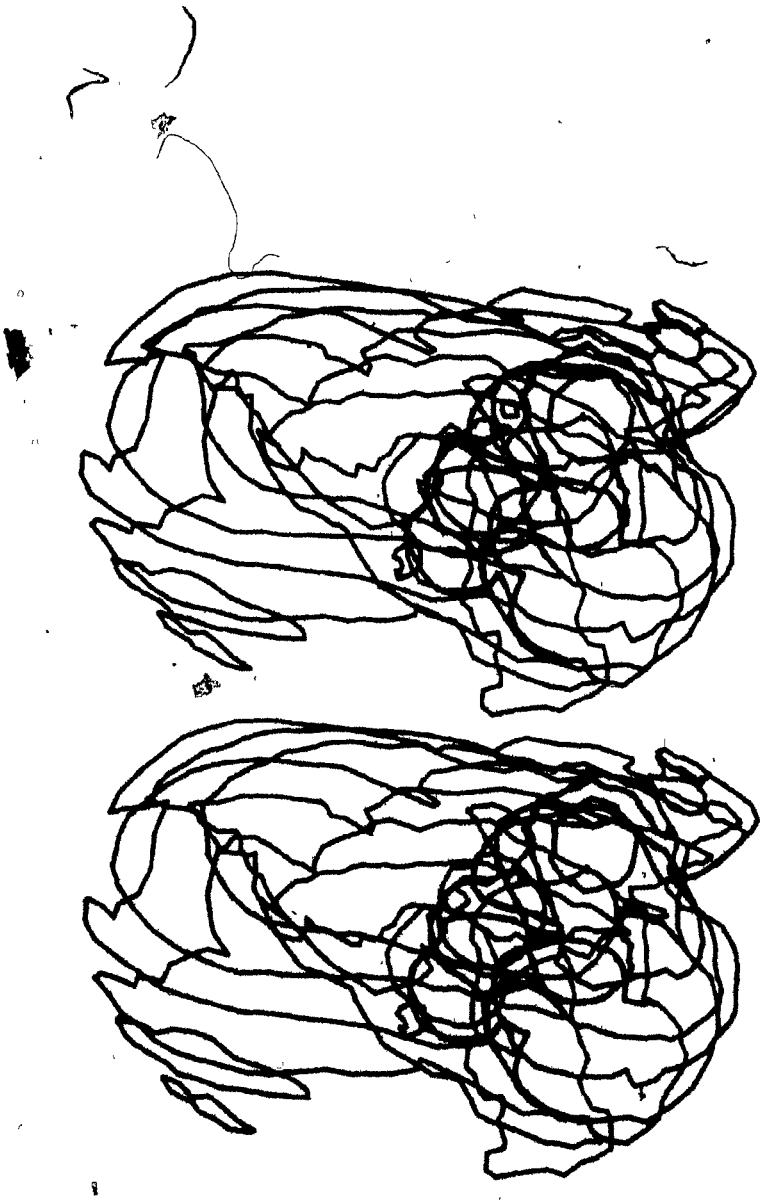

Fig. 4.7. A stereoscopic color display of lung 26A reconstructed. Blue contours pertain to the lung. Red contours indicate tumor nodules. Scale. 1:8.3

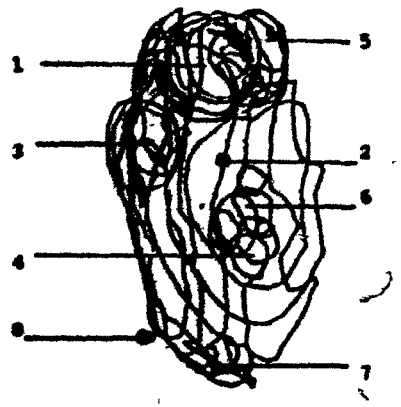

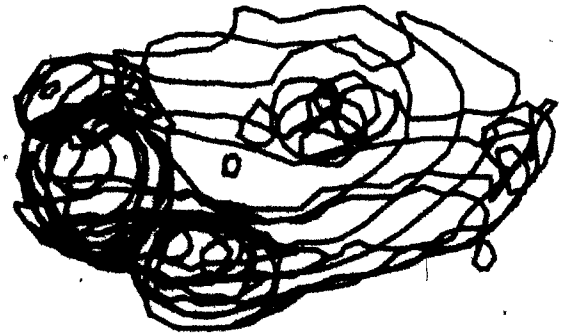

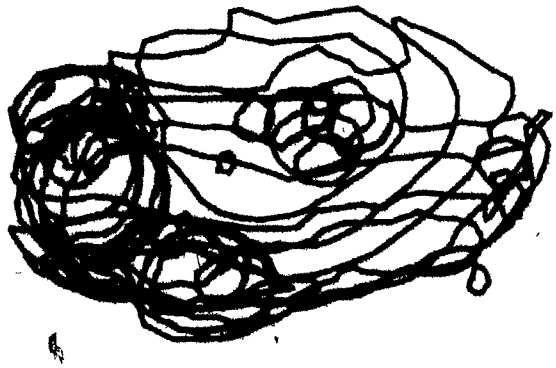

Table C. The volume, surface area and diameter (of an equivalent spheroid) of tumor nodules in Group I and Group II mice classified as peripheral and parenchymal tumors.

TABLE C

	GROUP I				GROUP II				TOTAL			
	No. of Tumors	Volume mm^3	Surface area mm^2	Diameter (mm)	No. of Tumors	Volume mm^3	Surface area mm^2	Diameter (mm)	No. of Tumors	Volume mm^3	Surface area mm^2	Diameter (mm)
Peripheral Tumors	18	0.41±0.56	3.65±0.37	0.79±0.36	15	3.95±5.81	21.38±34.33	1.51±0.84	33	2.02±4.26	11.73±24.6	1.12±0.77
Parenchymal Tumors	5	0.06±0.03	1.26±0.33	0.47±0.07	2	0.03±0.03	0.73±0.61	0.37±0.53	7	0.05±0.03	1.11±0.45	0.44±0.09
Total	23	0.33±0.52	3.13±3.93	0.72±0.34	17	3.49±5.57	20.26±32.62	1.38±0.96				

all.

The frequency with which individual diameters of tumor nodules occur, as grouped in class intervals of .4 mm is displayed in fig.4.8. The distribution of the diameters of Group I tumors is compared with the distribution of the diameters of the Group II tumors.

It is interesting to note that, with B-16 mouse melanoma cells growing as isolated spheroids in tissue culture, Folkman and Hochberg (11) reported a mean diameter ± standard deviation of approximately .84 ± .16 ml at 10 days, 1.5 ± .36 ml at 14 days and 1.76 ± .28 ml at 31 days. We obtained a mean diameter ± standard deviation of .72 ± .34 ml at 19 days and 1.38 ± .96 ml at 38 days.

Table D summarizes the data concerning the three dimensional spatial distribution of tumor nodules in the lung. For each lung, the mean nearest neighbor distance ± standard deviation is displayed. The mean nearest neighbor distance of tumor nodules may be compared with the mean nearest neighbor distance obtained by performing Monte Carlo Simulations and by computing the mean nearest neighbor distance for the theoretical distribution (infinite space). For each lung, 10 Monte Carlo trials were conducted to arrive at the mean nearest neighbor distance and the frequency distribu-

Fig. 4.8. The frequency (f) histogram of the diameter (D) (of an equivalent spheroid) of tumor nodules in Group I (continuous line) and Group II (broken chain line).

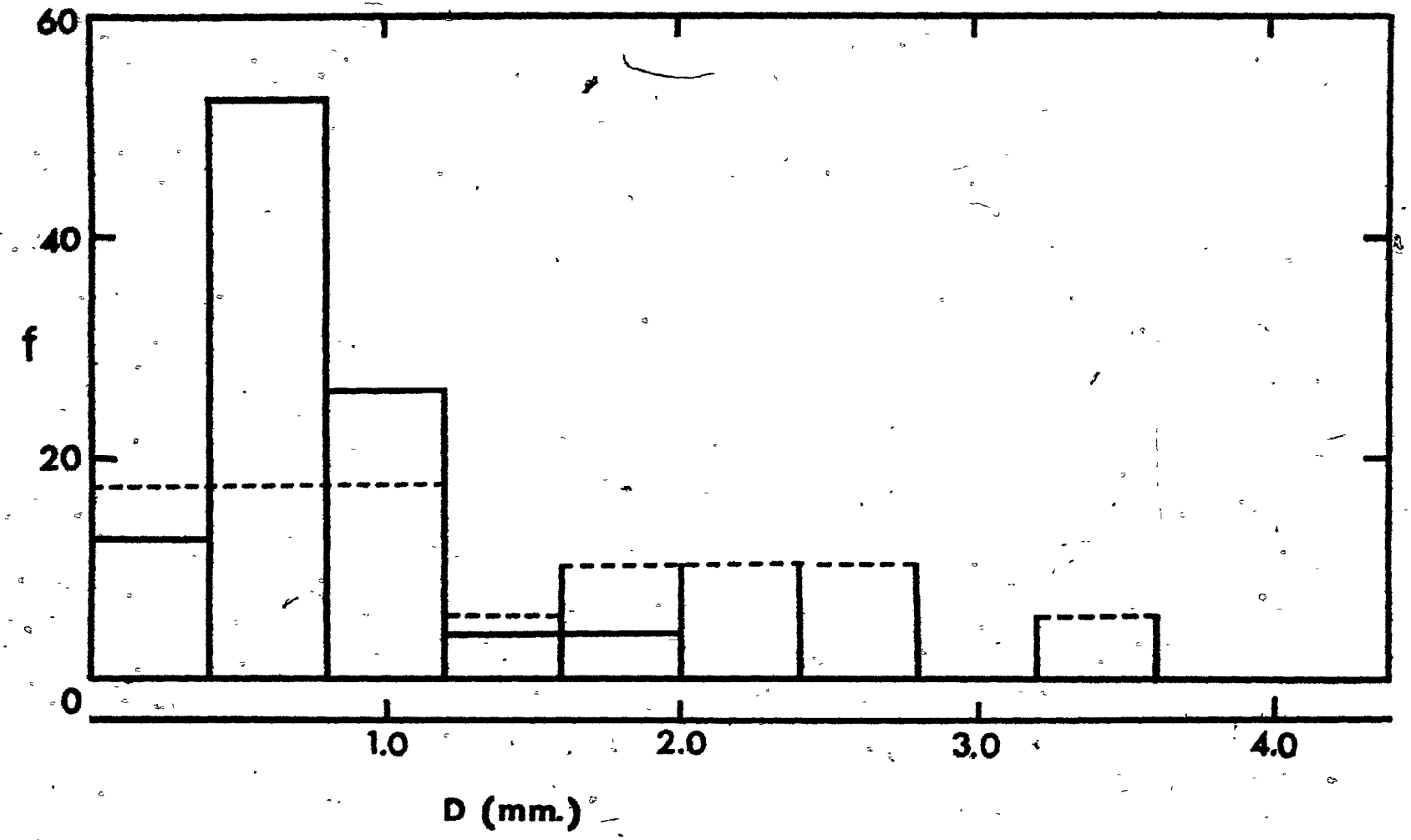
60
40
20
0
f
1.0
2.0
3.0
4.0
D (mm.)

Table D. The first nearest neighbor distance (mean ± standard deviation) of tumor nodules in experimental lungs compared with the nearest neighbor distance obtained by theoritical computation (infinite space) and by Monte Carlo simulations. In all but one lung (24A) the experimentally observed mean nearest neighbor distance of tumor nodules is larger than the mean nearest neighbor distance of the random three dimensional spatial distribution of tumor nodules.

TABLE D

FIRST NEAREST NEIGHBOUR DISTANCE (MM)

LUNG	NO. OF TUMOR NODULES	EXPERIMENTAL	RANDOM (SIMULATED)	RANDOM (INFINITE)
2A	9	1.13 ± 0.41	1.08 ± 0.60	0.89 ± 0.32
6A	3	3.69 ± 1.11	2.29 ± 0.62	1.45 ± 0.52
10A	11	1.79 ± 0.38	1.34 ± 0.61	1.10 ± 0.39
15A	4	4.14 ± 0.68	2.22 ± 1.01	1.54 ± 0.56
24A	5	1.64 ± 0.47	1.71 ± 0.78	1.28 ± 0.46
26A	8	1.52 ± 0.49	1.31 ± 0.70	0.91 ± 0.33

tion of the nearest neighbor distances. An additional 40 trials were conducted to study lung 10A more closely. In all but one lung (15A) the experimental nearest neighbor distance was greater than the simulated nearest neighbor distance which in turn was greater than the theoretical nearest neighbor distance. The 'boundary effect' of the irregularly shaped lung on the spatial distribution of tumor nodules is reflected in the finding that the simulated nearest neighbor distance is greater than the theoretical nearest neighbor distance.

Figs.4.9 - fig.4.14 are displayed the frequency distribution diagrams of the nearest neighbor distances of tumor nodules for each lung. The frequency distribution obtained from Monte Carlo simulations (10 trials conducted for all lungs except 10A for which 50 trials were performed) is compared with the theoretical distribution (for infinite space) and the experimental nearest neighbor distance distribution. The frequency histogram of observed values of the mean nearest neighbor distance for each of the 50 simulations performed for lung 10A is shown in fig.4.15. This histogram indicates that the probability of occurence of the experimentally observed mean nearest neighbor distance is about 2%.

Fig. 4.9. The frequency (F) distribution of the nearest neighbor distances (R) of tumor nodules in lung 2A is compared with the frequency distribution of the mean nearest neighbor distances of tumor nodules generated randomly. The unshaded histograms represent the experimental data and the cross-hatched histograms represent data obtained from Monte Carlo simulations (10 trials). The smooth curve depicts the frequency distribution of the nearest neighbor distances of tumor nodules distributed randomly in infinite space.

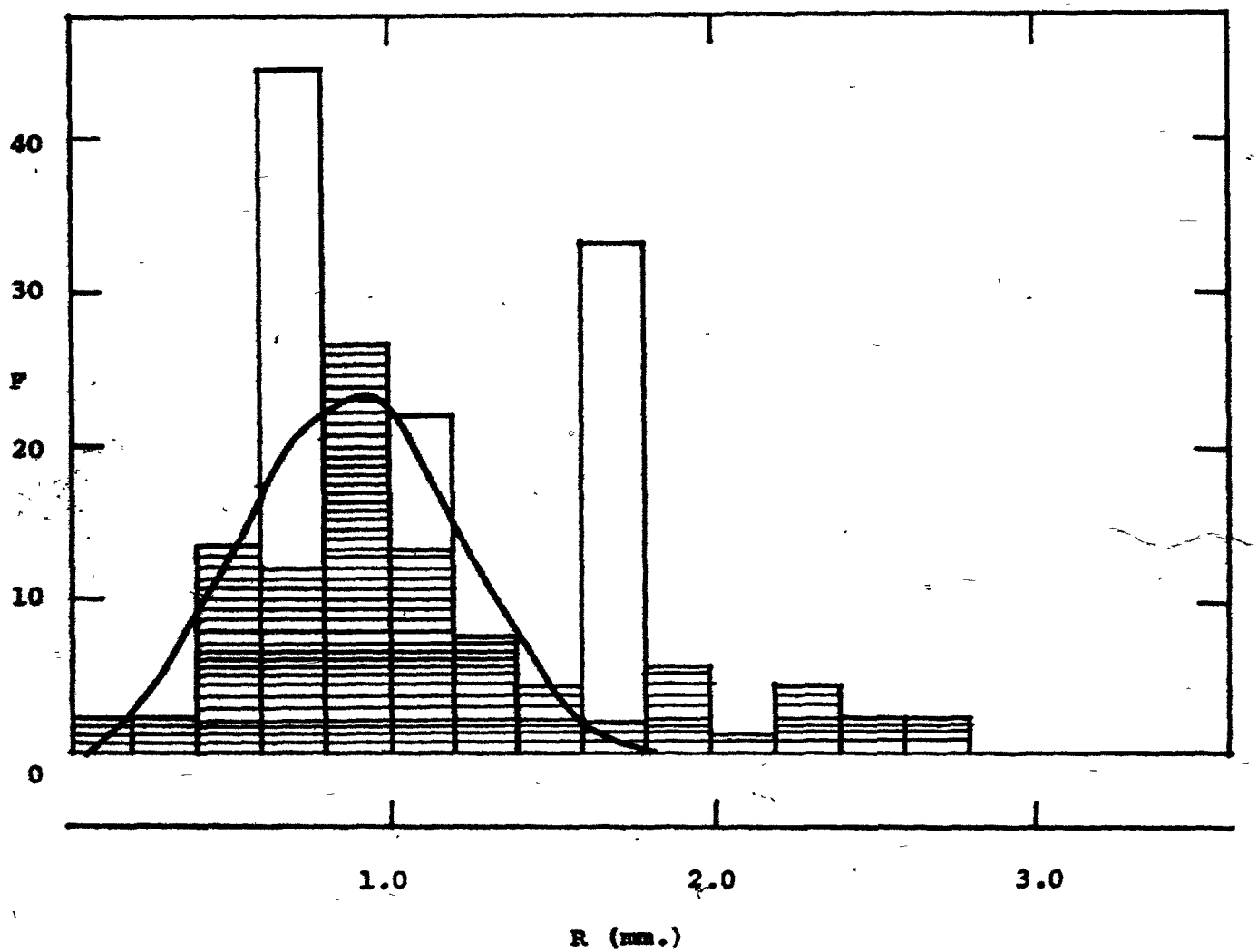
40
30
F
20
10
0
1.0
2.0
3.0
R (mm.)

Fig. 4.10. The frequency (F) distribution of the nearest neighbor distances (R) of tumor nodules in lung 6A is compared with the frequency distribution of the mean nearest neighbor distances of tumor nodules generated randomly. The unshaded histograms represent the experimental data and the cross-hatched histograms represent data obtained from Monte Carlo simulations (10 trials). The smooth curve depicts the frequency distribution of the nearest neighbor distances of tumor nodules distributed randomly in infinite space.

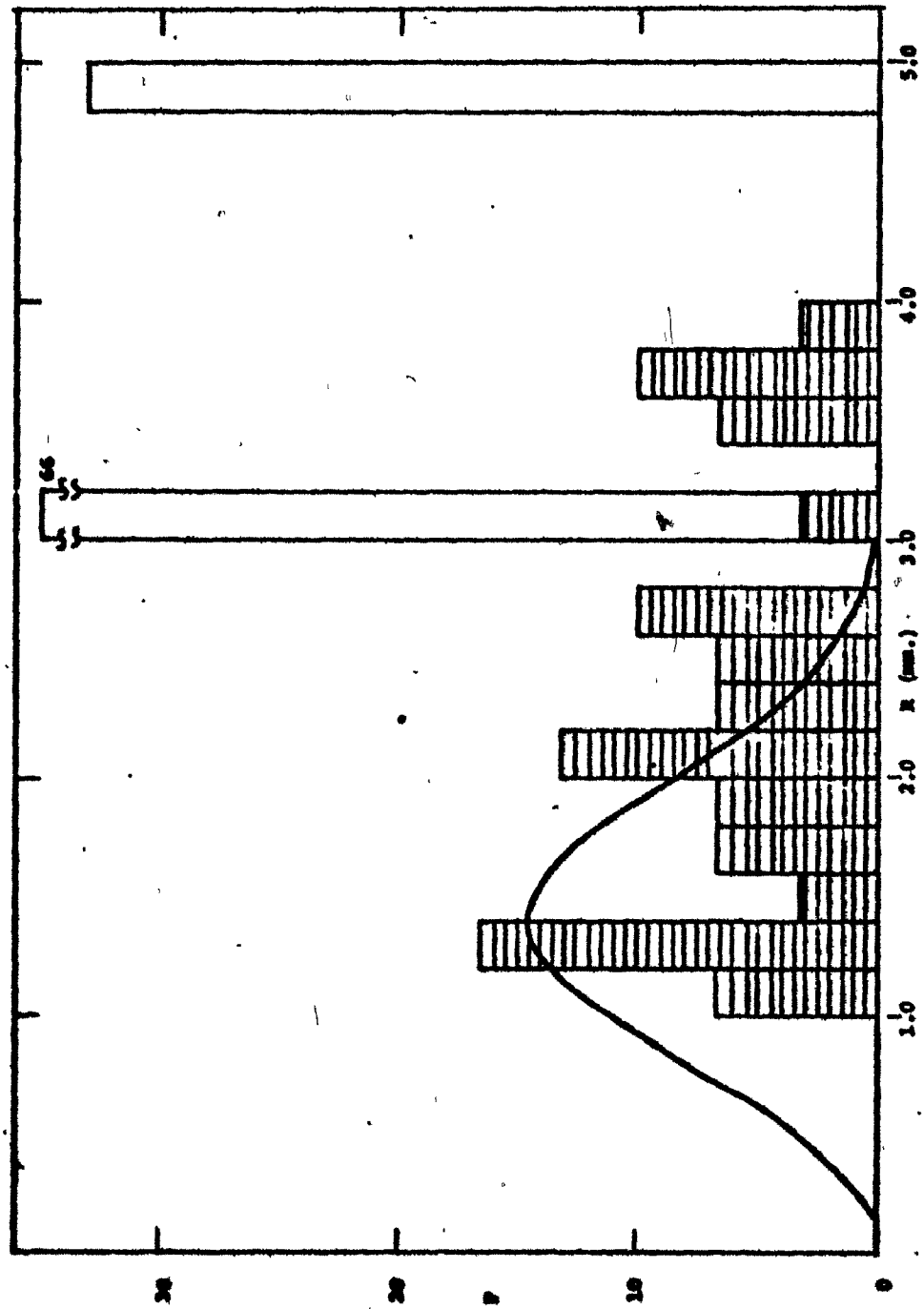
5.0
4.0
3.0
2.0
1.0
r (mm.)

Fig. 4.11. The frequency (f) distribution of the nearest neighbor distances (R) of tumor nodules in lung 10A is compared with the frequency distribution of the mean nearest neighbor distances of tumor nodules generated randomly. The unshaded histograms represent the experimental data and the cross-hatched histograms represent data obtained from Monte Carlo simulations (50 trials). The smooth curve depicts the frequency distribution of the nearest neighbor distances of tumor nodules distributed randomly in infinite space.

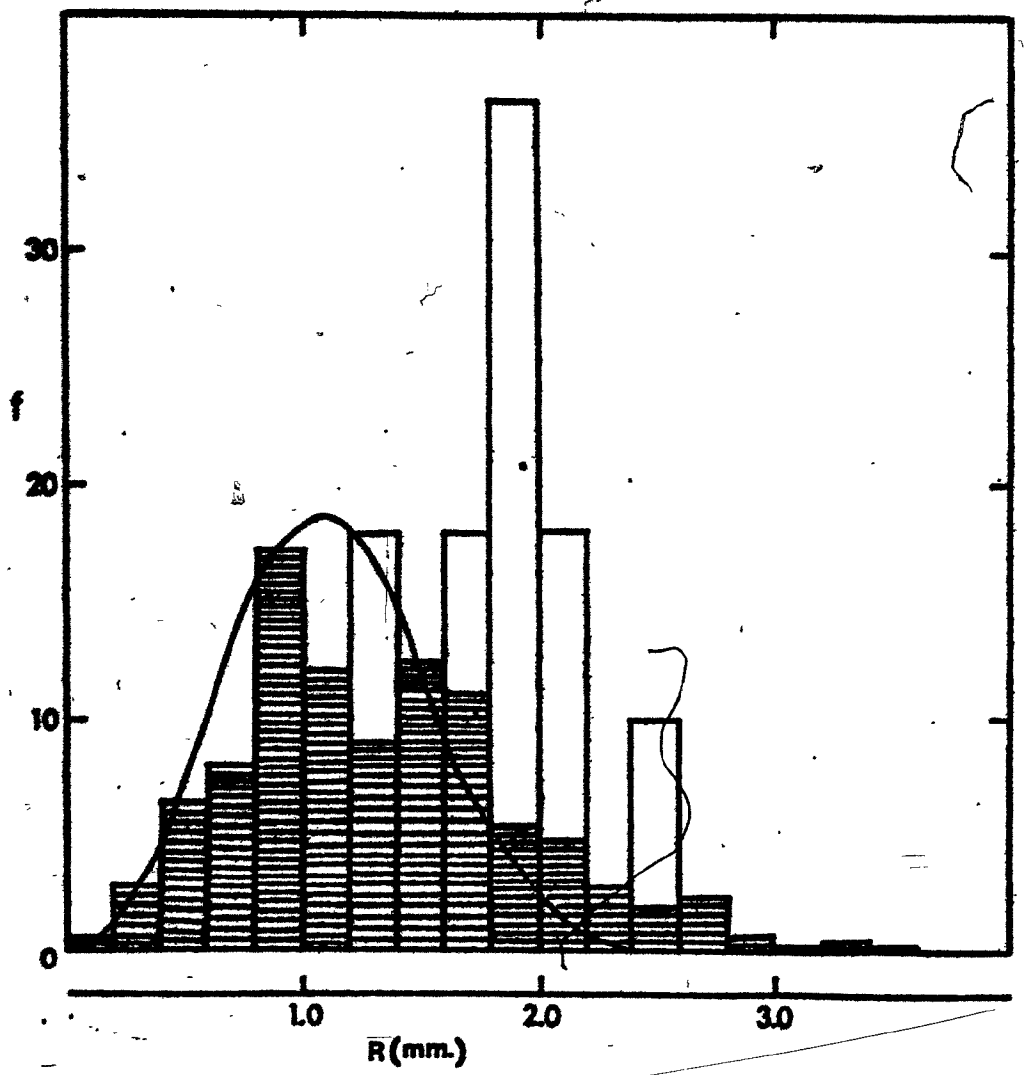
30
20
10
0
f
1.0
2.0
3.0
R(mm.)

Fig. 4.12. The frequency (F) distribution of the nearest neighbor distances (R) of tumor nodules in lung 15A is compared with the frequency distribution of the mean nearest neighbor distances of tumor nodules generated randomly. The unshaded histograms represent the experimental data and the cross-hatched histograms represent data obtained from Monte Carlo simulations (10 trials). The smooth curve depicts the frequency distribution of the nearest neighbor distances of tumor nodules distributed randomly in infinite space.

5.0
4.0
3.0
2.0
1.0
0.4
0
R (mm.)

Fig. 4.13. The frequency (F) distribution of the nearest neighbor distances (R) of tumor nodules in lung 24A is compared with the frequency distribution of the mean nearest neighbor distances of tumor nodules generated randomly. The unshaded histograms represent the experimental data and the cross-hatched histograms represent data obtained from Monte Carlo simulations (10 trials). The smooth curve depicts the frequency distribution of the nearest neighbor distances of tumor nodules distributed randomly in infinite space.

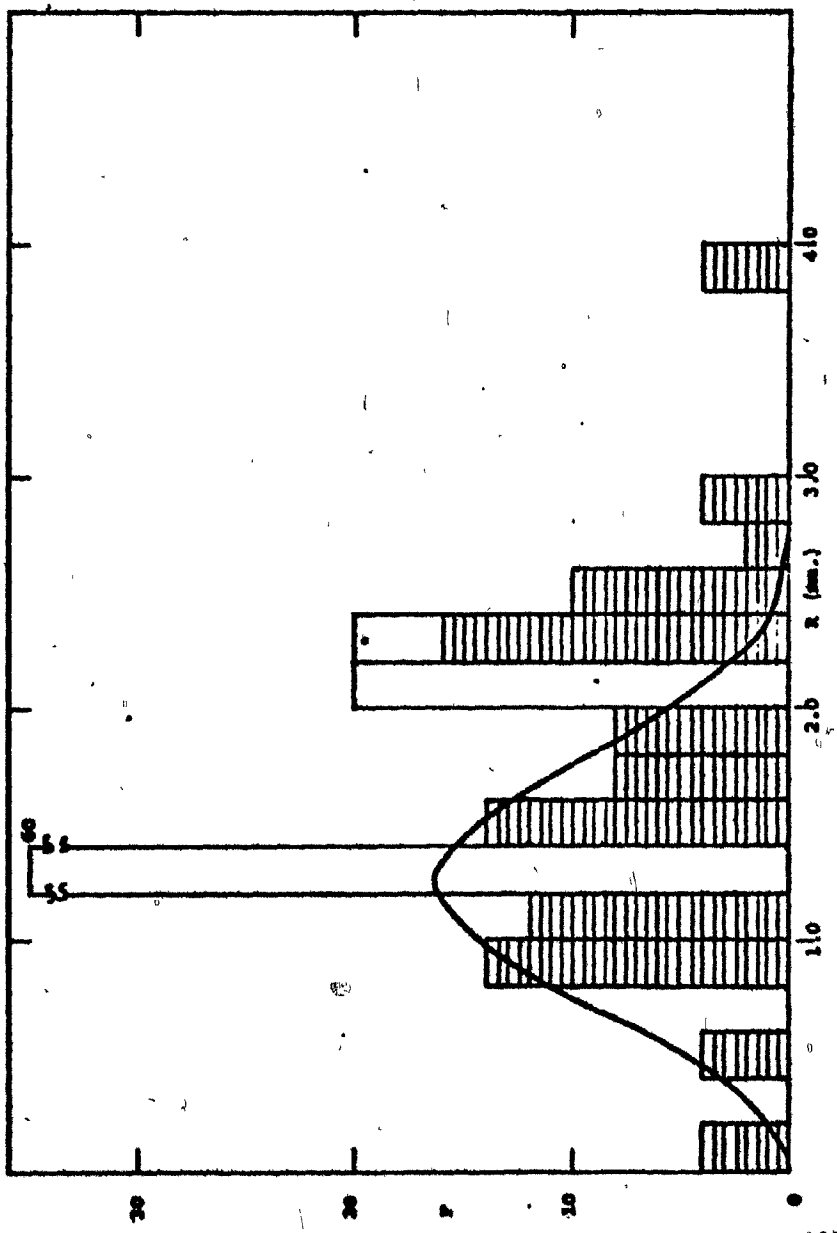
4.0
3.0
2.0
1.0
x (mm.)

Fig. 4.14. The frequency (F) distribution of the nearest neighbor distances (R) of tumor nodules in lung 26A is compared with the frequency distribution of the mean nearest neighbor distances of tumor nodules generated randomly. The unshaded histograms represent the experimental data and the cross-hatched histograms represent data obtained from Monte Carlo simulations (10 trials). The smooth curve depicts the frequency distribution of the nearest neighbor distances of tumor nodules distributed randomly in infinite space.

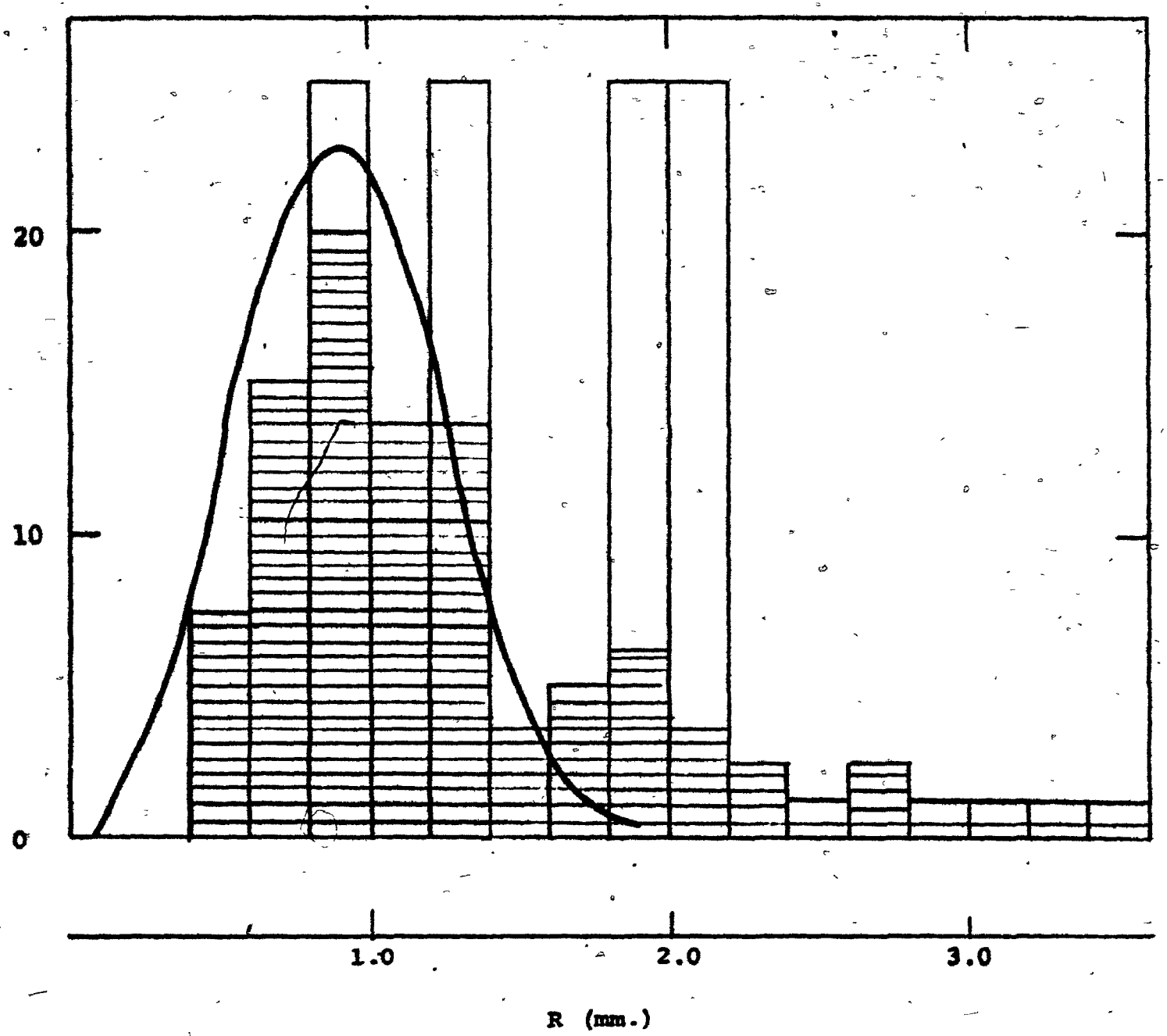
20
10
0
1.0
2.0
3.0
R (mm.)

Fig. 4.15. The frequency (f) histogram of observed values of the mean nearest neighbor distance (R) for each of the 50 simulations performed for lung 10A is displayed. On the basis of this histogram the experimentally observed mean nearest neighbor distance (1.79 mm.) for lung 10A would have a probability of occurrence of about 2%.

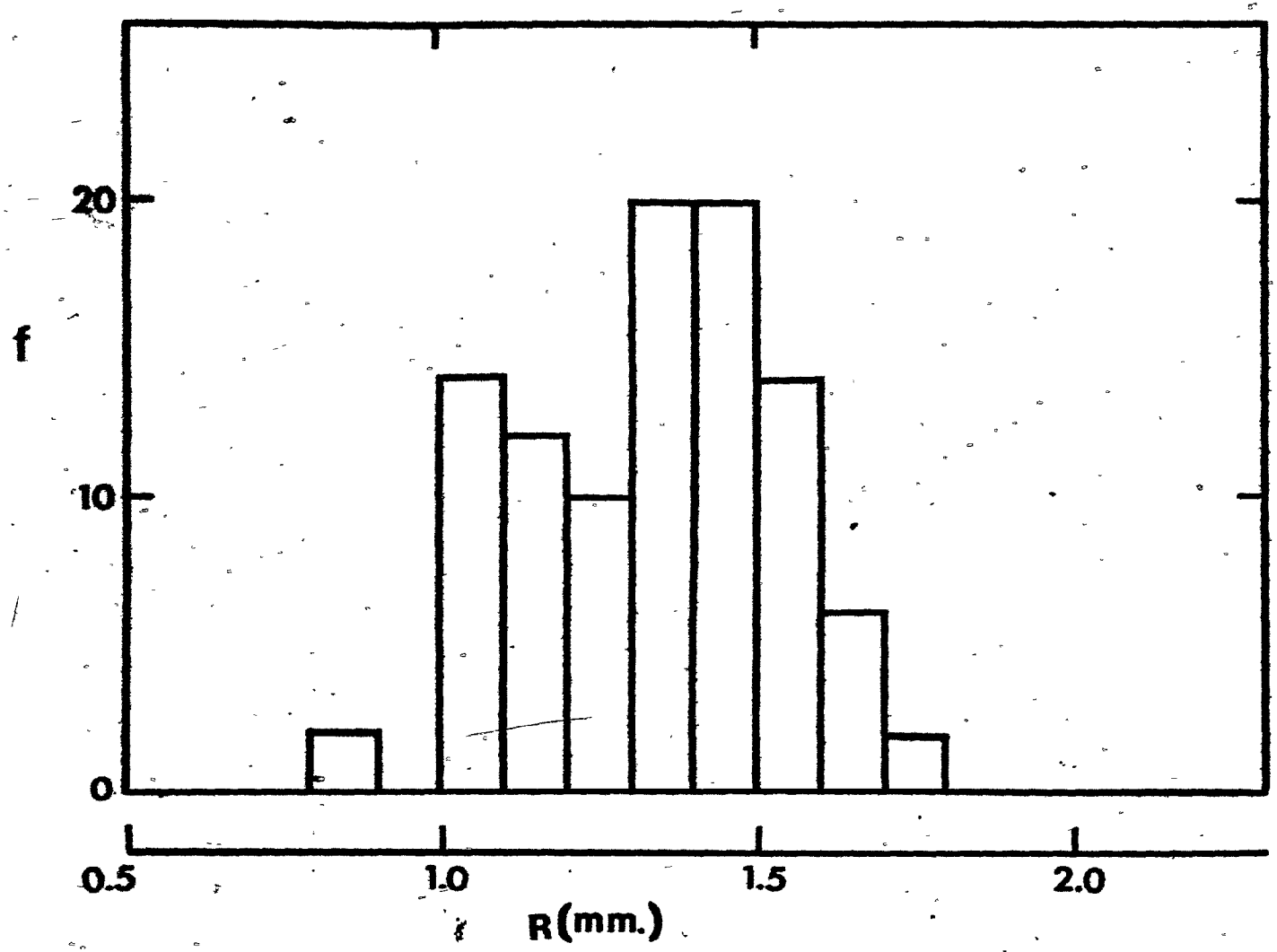
20
10
0
f
0.5
1.0
1.5
2.0
R(mm.)

4.5 Discussion.

Our results give a strong indication that the three dimensional spatial distribution of tumor nodules in the lung may be non-random. This follows from the fact that tumor nodules are largely peripheral and that the mean nearest neighbor distance of tumor nodules in one experimental lung differs significantly from the same distance in a random spatial distribution of tumor nodules.

There is a wide difference in the size of tumor nodules in the individual lungs as well as between different lungs. Also, the parenchymal tumor nodules are considerably smaller than the peripheral tumor nodules. We observe a much greater variability in the size distribution than in the in vitro study (11). The increased variability in the in vivo system might arise from atleast 3 different mechanisms:

a. The nodules might act as continuous sources for generating secondary metastatic spread. In this case, the small nodules that are found might represent a younger class than the larger nodules.

b. The growth of a tumor nodule depends on its microenvironment. Thus different tumor sizes result from a wide variation in the ability of tumor nodules to become vascularized and/or the effect of various extrinsic factors on their growth kinetics.

c. Nodules may be initiated by either single cells or emboli of different sizes.

Folkman and Brem (6) have demonstrated that the growth of solid tumors is inhibited by the presence of a cartilage source in the vicinity of the tumor nodules. A diffusible inhibitory factor was shown to inhibit capillary proliferation induced by tumor angiogenesis factor (TAF). The inhibitory effect operates over distances of up to 2.0 mm (in vivo) preventing or delaying the vascularization of tumor nodules. The parenchymal tumors would be particularly susceptible to such inhibitory effect due to the fact that the cartilagenous branchial network is much more profuse toward the center of the lung. At the present moment it is not possible to evaluate the relative importance of these mechanisms.

The three-dimensional reconstruction technique we have used has the potential for greatly expanding the quantitative data base for questions of considerable importance in the study of metastasis, such as: assessing the relative importance of secondary and tertiary tumor spread; determining the influence of the primary tumor on the growth of secondary tumors; and determining the spatial dependence of the mitotic index as a function of metastatic size and location before and after chemotherapy.

REFERENCES

1. Ahuja, D. C. and Coons, S. A. Geometry for Construction and Display. IBM Syst. J., vol. 7, nos 3 and 4: 188-205, 1968.

2. Barry, C. D., Ellis, R. A., Graesser, S. M. and Marshall, G. R. Display and Manipulation in Three Dimensions. In: M. Faiman and J. Nievergelt (eds.), Pertinent Concepts in Computer Graphics, pp. 104-133. Urbana: University of Illinois Press, 1969.

3. Baserga, R., Putong, P. B., Tyler, S. and Wartman, W. B. The Dose-Response Relationship Between the Number of Embolic Tumor Cells and the Incidence of Blood-Borne Metastases. Cancer Res., 20: 173-184, 1960.

4. Boeryd, B., Ganelius, T., Lundin, P., and Mellgren, J. Counting and Sizing of Tumor Metastases in Experimental Oncology. Int. J. Cancer, 1: 497-502, 1966.

5. Bond, J. P. Interactive Computer Graphics and Macromolecular Structures. SIGGRAPH-ACM, 6,4:13-17, 1972.

6. Brem, H. and Folkman, J. Inhibition of Tumor Angiogenesis Mediated by Cartilage. J. Exp. Med., 141: 427-439,

1975.

7. Coman, D. R. Mechanisms Responsible for the Origin and Distribution of Blood-Borne Tumor Metastases: A Review. Cancer Res., 13: 397-404, 1953.

8. Dempster, W. T. Paraffin Compression due to the Rotary Microtome. Stain Technology, vol. 18, No. 1: 13-24, 1943.

9. Fidler, J. I. Patterns of Tumor Cell Arrest and Development. In: L. Weiss (ed.), Fundamental Aspects of Metastasis, pp. 275-289. Amsterdam: North-Holland Publishing Co., 1976.

10. Fisher, B. and Fisher, E. R. The Organ Distribution of Disseminated 51Cr-labeled Tumor Cells. Cancer Res., 27: 412-420, 1967.

11. Folkman, J. and Hochberg, M. Self Regulation of Growth in Three Dimensions. J. Exp. Medicine, 138: 745-753, 1973.

12. Folkman, J. Tumor Angiogenesis Factor. Cancer Res., 34: 2109-2113, 1974.

13. Fox, C. A. and Bannard, J. W. A Quantitative Study of the Purkinje Cell Dendrite Branchlets and their Relation to Afferent Fibres. J. Anat., 91: 299-313, 1957.

14. Gaunt, W. A. and Gaunt, P. N. In: W. A. Gaunt and P. N. Gaunt (eds.), Three Dimensional Reconstruction in Biology, pp. 1-5. Maryland: University Park Press, 1978.

15. Heard, O. O. Section Compression Photographically Rectified. Anat. Rec., 109: 745-755, 1951.

16. Johnson, R. Notes on the Vascular Physiology of Primary Tumors and Micrometastases. In: L. Weiss (ed.), Fundamental Aspects of Metastasis, pp. 253-273. Amsterdam: North-Holland Publishing Co., 1976.

17. Julesz, B. In: B. Julesz (ed.), Foundations of Cyclopean Perception, pp. 142-183. Chicago and London: The University of Chicago Press, 1971.

18. Kendall, M. G. and Moran, P. A. P. In: M. G. Kendall (ed.), Geometrical Probability, pp. 47-48. London: Charles Griffin and Co. Ltd., 1963.

19. Khato, J. et al. Quantitative Studies on Lung Metastases with Reference to the Number and Size of Tumor Nodules produced by Intravenous Inoculation of Tumor Cells. Sci. Rep. Res. Inst. Tohoku Univ. C, vol. 22, No. 3-4: 69-76, 1975.

20. Ledley, R. S. High Speed Automatic Analysis of Biomedical Pictures. Science, 146: 216-222, 1964.

21. Levinthal, C. et al. Graphics in Macromolecular Chemistry. In: J. Nievergelt, and D. Secrest, Eds.), Emerging Concepts in Computer Graphics, pp. 231-242. New York: W. A. Benjamin, Inc., 1969.

22. Levinthal, C. and Ware, R. W. Three Dimensional Reconstruction from Serial Sections. Nature, 236: 207-210, 1970.

23. Levinthal, C., Macagno, E. and Tountas, C. Computer Aided Reconstruction from Serial Sections. Federation Proceedings, 33: 2336-2340, 1974.

24. Liotta, L. A., Kleinerman, J. and Saidel, G. M. Quantitative Relationship of Intravascular Tumor Cells, Tumor Vessels and Pulmonary Metastases following Tumor Implantation. Cancer Res., 34: 997-1004, 1974.

25. Liotta, L. A. and DeLisa, C. Method for Quantitating Tumor Cell Removal and Tumor Cell Invasive Capacity in Experimental Metastases. Cancer Res., 37: 4003-4008, 1977.

26. Liotta, L. et al. In Vivo Monitoring of the Death Rate of Artificial Murine Pulmonary Micrometastases. Cancer Res., 38: 1231-1236, 1978.

27. Lodin, Z., Nemec, V., Kerasek, J. and Skrivanova, P. Studies on the Effect of Fixation on Nervous Tissue. II. Changes of sizes of nuclei of nervous cells after fixation

and further histological treatment of the nervous tissue. Acta histochem., Bd. 28, S: 297-312, 1967.

28. Lucke, B. et al. Differential Growth of Metastatic Tumors in Liver and Lung. Experiments with Rabbit V2 Carcinoma. Cancer Res., 12: 734-738, 1952.

29. Mellgren, J. Quantitation of Metastases in Experimental Animals. In: L. Weiss (ed.), Fundamental Aspects of Metastasis, pp. 243-252. Amsterdam: North-Holland Publishing Co., 1976.

30. Newman, W. M. and Sproull, R. F. Three Dimensional Transformations and Perspective. In: W. M. Newman and R. F. Sproull (eds.), Principles of Interactive Computer Graphics, pp. 235-265. New York: McGraw Hill Book Co., 1973.

31. Nicolson, G. L., Winkelhake, J. L. and Nursey, A. C. An Approach to Studying the Cellular Properties Associated with Metastasis: Some in vitro properties of tumor variants selected in vivo for enhanced metastasis. In: L. Weiss (ed.), Fundamental Aspects of Metastasis, pp. 291-303. Amsterdam: North-Holland Publishing Co., 1976.

32. Paget, S. The Distribution of Secondary Growth in Cancer of the Breast. Lancet, 1: 571-573, 1889.

33. Reeder, C. M. M. and Tilly, R. Three Dimensional

Reconstruction of Nervous Tissue. In: Stereology, pp. 310-311, Proc. of the second Int. Cong. for Stereology, Chicago, 1967.

34. Proctor, J. W., Auclair, B. G. and Rudenstam, C. M. The Distribution and Fate of Blood-Borne 125IUdR-labeled Tumor Cells in Immune Syngeneic Rats. Int. J. Cancer, 18: 255-262, 1976.

35. Reddy, D. R. et al. Computer Analysis of Neuronal Structure. In: S. B. Kater and C. Nicholson (eds.), Intracellular Staining Techniques in Neurobiology, pp. 227-254. New York: Springer-Verlag, 1973.

36. Rule, J. T. and Watts, R. F. In: J. T. Rule and R. F. Watts (eds.), Engineering Graphics, pp. 150-183. New York: McGraw Hill Book Co., 1951.

37. Saidel, G. M., Liotta, L. A. and Kleinerman, J. System Dynamics of a Metastatic Process from an Implanted Tumor. J. Theor. Biol., 58: 417-434, 1976.

38. Shymko, R. M. and Glass, L. Cellular and Geometric Control of Tissue Growth and Mitotic Instability. J. Theor. Biol., 63: 355-374, 1976.

39. Simpson-Herren, L., Sanford, A. H. and Holmquist, J. P. Cell Population Kinetics of Transplanted and Metastatic Lewis Lung Carcinoma. Cell Tissue Kinet., 7: 349-361,

1974.

40. Sjostrand, F. S. In: F. S. Sjostrand (ed.), Electron Microsdopy of Cells and Tissues, pp. 232-370. New York: Academic Press, 1967.

41. Smith, A. Tissue Shrinkage by Attachment of Paraffin Sections to Slides: its effects on staining. Stain Technology, 37: 339-345, 1962.

42. Weiss, L. Introduction. In: L. Weiss (ed.), Fundamental Aspects of Metastasis, pp. 1-5, Amsterdam: North-Holland Publishing Co., 1976.

43. Wexler, H. Accurate Identification of Experimental Pulmonary Metastases. J. nat. Cancer Inst., 36: 641-645, 1966.

44. Wicksell, S. D. The Corpuscle Problem. A mathematical study of a biometric problem. Biometrika, 17: 84-99, 1925.

45. Wicksell, S. D. The Corpuscle Problem. Case of ellipsoidal corpuscles. Biometrika, 18: 151-172, 1926.

46. Wood, J. S. et al. An Experimental Study of the Relationship between Tumor Size and Number of Lung Metastases. Cancer, 7: 437-443, 1954.

47. Zeidman, I., McCutcheon, M. and Coman, D. R. Factors

Affecting the Number of Tumor Metastases: Experiments with a Transplantable Mouse Tumor. Cancer Res., 10: 357-359, 1950.

48. Zeidman, I. The Fate of Circulating Tumor Cells. I. Passage of cells through capillaries. Cancer Res., 21: 38-39, 1961.

APPENDIX A

A.1 The Primary And Secondary File Data Structure.

a. The Primary File (fig.2.4).

Record number 1 contains the table, INFOR such that:

INFOR(1) = The last section digitized.

INFOR(2) = unused

INFOR(3) = Address to store the next contour in.

INFOR(4) = The number of sections in the lung.

INFOR(5) = The number of structures in the lung.

INFOR(6) = The lung identification number.

Record number 5 contains the table, ZTAB, such that:

ZTAB(I) = The Z-coordinate of section number 'I'.

Record numbers 2,3,4 and 6 are presently unused.

Structures are assigned record numbers 7 to 70. Each such record contains the table, CONAD, such that:

CONAD(I) = The address of contour in section number 'I'.

b. The Secondary File (fig.2.5).

Each list of X, Y coordinates representing a contour is preceded by a header zone as shown in fig.A.1. The header zone is followed by the X and Y coordinates of the first point, then the X and Y coordinates of the second point, and so on. The header zone contains the following elements:

NUM = The number of coordinate points recorded in the contour

ICON = THE structure number corresponding to the contour.

IARE = The area enclosed by the contour.

IPER = The perimeter of the contour.

IXCG = The X-coordinate of the center of mass of the contour.

IYCG = The Y-coordinate of the center of mass of the contour.

A.2 Quantitation Of The Volume And Surface Area Of Tumor Nodules: Error Estimates.

To test the accuracy in the computation of the volume and surface area of the tumor nodules the following test was conducted.

Serial section contours of a sphere (10 cm radius) were

Fig. A.1. The storage of the list of X, Y coordinates of points along a contour is preceded by the header zone. The header zone consists of six words labelled NUM, ICON, IAREA, IPER, IXCG, IYCG. (See text for the definition of these words.)

NUM	Y	X	Y
ICON	X	Y	X
IARE	Y	X	Y
IPER	X	Y	X
IXCG	Y	X	Y
IYCG	X	Y	X
X	Y	X	Y
Y	X	Y	X
X	Y	X	Y
Y	X	Y	X
X	Y	X	Y
Y	X	Y	X
X	Y	X	Y
Y	X	Y	X
X	Y	X	Y

STORAGE OF DATA (IN THE SECONDARY FILE)

CONCERNING ANY CONTOUR

digitized in accordance with the data acquisition procedures. 19 sections (parallel to each other) spaced 1 cm apart were digitized. The volume and surface area of the sphere was computed by the computer algorithm (Chapter III). These estimates are compared with the theoretical computation of the volume and surface area of the sphere. Table A.2 displays these computations.

The computation of the volume of the sphere (by use of the computer algorithm) was underestimated by 1.66%. The surface area of the sphere was underestimated by 5.45%.

Table A.2. The volume and surface area of a sphere computed by the computer algorithms is compared with the theoritical computations. The computer algorithms under estimate the volume of the sphere by 1.66% and the surface area by 5.45%.

TABLE A.2

	THEORITICAL COMPUTATION (X)	ESTIMATED BY COMPUTER ALGORITHMS (Y)	% ERROR $\frac{(X-Y)}{X} * 100$
VOLUME OF SPHERE (V)	4180 cm^3	4110.56 cm^3	1.66%
SURFACE AREA OF SPHERE (S)	1256 cm^2	1187.54 cm^2	5.45%

APPENDIX B

B.1 Quantitative Analysis And Associated Problems.

The quantitative analysis programs compute the volume, surface area and sphericity index of the tumor nodules. In addition, we computed the cross-sectional width (w) of the tumor nodules from the computer print out of the sections. The length (L) of the tumor nodules was computed by counting the number of sections the tumor nodule goes through.

It was observed that the width (w) consistently exceeded the length (L) in all tumor nodules (in all lungs) under study. Assuming a random orientation of tumor nodules there should be a 50% chance of observing that the length of the tumor nodules exceed the width. To investigate this anamolous situation we set about examining the artifacts of serial sectioning more closely.

It has been recognized (8,14,40,41) that artifacts encountered during histological sectioning impair 3-D reconstruction. Experiments (8,27) to determine which factors increase and which decrease the distortion have been performed. The conditions under which minimal distortion re-

sults, have also been outlined. However, work on 3-D reconstruction from serial sections (22,35) do not consider these artifacts.

Previous studies (8,40) indicate that during serial sectioning, a paraffin block undergoes compression. The compression of the paraffin block is manifest both along the surface of the cut-section (ie in the plane of cutting) and in the direction perpendicular to the plane of cutting. Along the surface of the cut-section compression leads to an overall shrinkage of the material. Compression perpendicular to the plane of cutting results in section thickness being greater than would be expected from the microtome setting. The extent of compression is dependent on the embedding medium, the cutting temperature, and the bevel and rake angle of the microtome knife (8).

The extent of compression along the plane of cutting can be quantified by determining the shrinkage of the distance between any two points on the surface of the section. The compression in the direction perpendicular to the plane of cutting can be computed from the number of serial sections obtained for any given thickness of the paraffin block.

Experiments were conducted to determine the extent of

compression. In all experiments a paraffin block (containing the upper left lobe of mice lung) was initially frozen (to about -5 degrees centigrade) and mounted on an American Optical Corporation "820" Spencer microtome. The microtome was set to cut serial sections 8 microns in thickness. A vernier calliper (resolution of .05 mm) was used to measure the position of the block face with respect to a fixed reference. Measurements were taken from the four corners of the block surface (fig.B.1). The average of these measurements constitutes the position of the block with respect to the fixed reference. The distances A, B, C (fig.B.1) between the positions of the sciatic nerves on the block face were also measured with the vernier calliper.

Experiments I and II were conducted to evaluate the extent of compression under the conditions under which serial sectioning was normally undertaken. During the sectioning procedure the paraffin wax gradually softens rendering further sectioning difficult. Consequently, the block is removed from the microtome to continue serial sectioning. This process is repeated until the entire lung is sectioned. Prior to freezing/refreezing the block, the position of the block face is measured and the number of usable sections obtained is counted. At this point, the distances A, B, C are also measured. Damaged sections produced either due to imperfections in the knife edge or due to the rapid softening

Fig. B.1. The distance of the block surface is measured with respect to the block support. Four measurements-1, 2, 3, 4 are used to arrive at the mean block thickness.

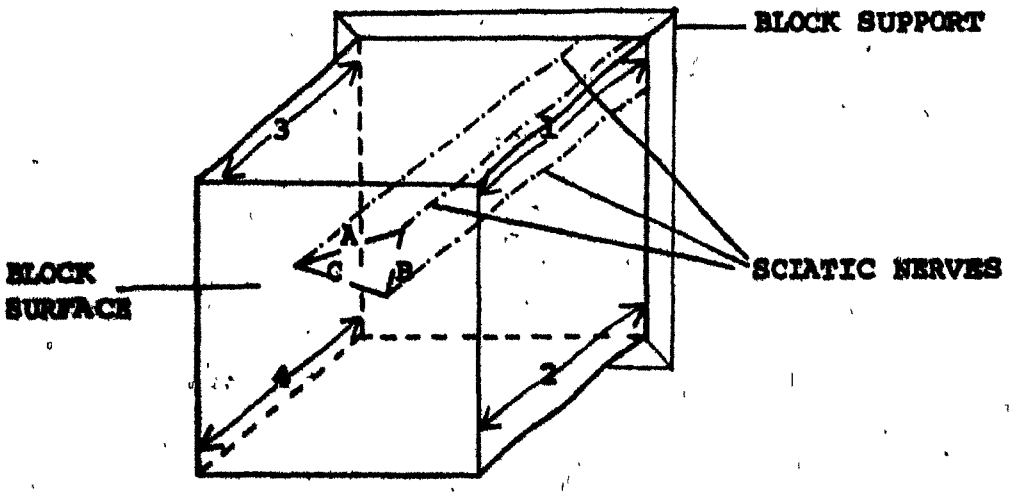

[illegible] BLOCK MOUNTED ON MICROTOME

of the wax are not counted. Also, refreezing of the block results in the misalignment of the block face with respect to the knife edge. Every time the block is returned to the microtome (after refreezing) it may need trimming to align its surface to the knife edge. Sections that are damaged and material lost in serial sectioning does not appear on the histological slides and contributes to compression errors. Data obtained during experiment I and II is displayed graphically (fig.B.2)

B.2 Compression Error Along The Axis Normal To The Plane Of Cutting.

Data obtained from Experiments I and II is displayed graphically in fig.B.2. The position of the block face measured relative to a fixed reference is plotted along the ordinate and the cumulative number of sections obtained for respective positions of the block face is plotted along the abscisse. The compression error can be easily computed from the relationship exhibited between these two variables (fig.B.2).

Let N denote the cumulative number of sections, n be the number of microtome strokes, y the position of the block face with respect to a reference (in mm), and x be the cumulative number of sections obtained until position y. Since,

Fig. B.2. Data obtained from Experiment I (marked △) and Experiment II (marked □) is displayed graphically. The abscissa X is the cumulative number of sections and the ordinate Y is the position of the block face in mm. Regression lines are drawn through the data for each experiment. The compression error is 37.89% for Experiment I and 31.45% for Experiment II.

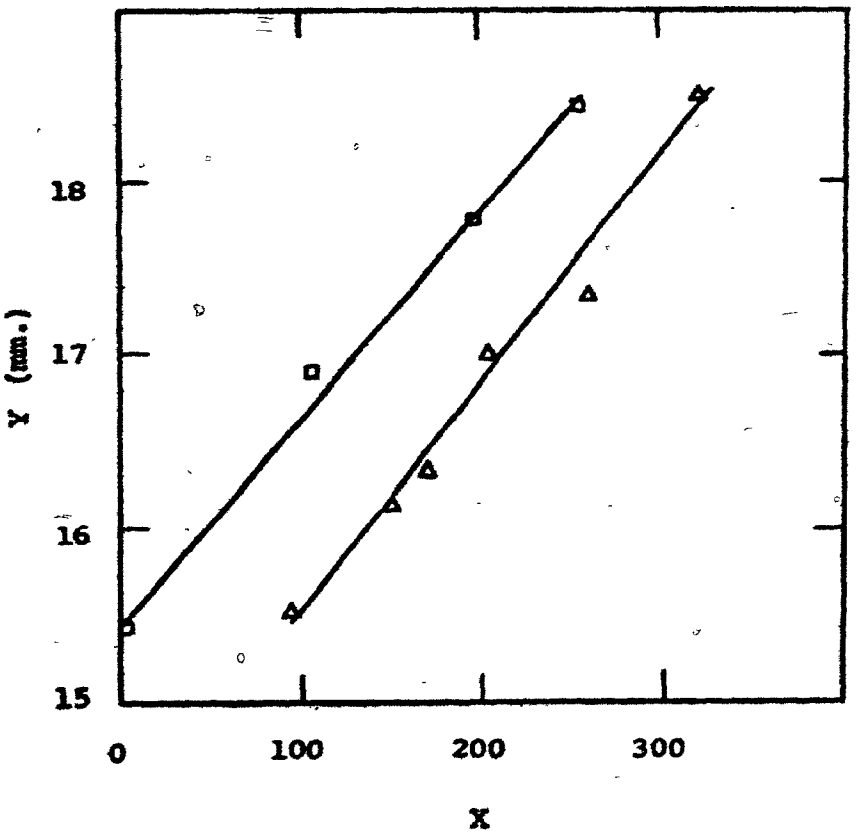
18
17
16
15
Y (mm.)
0
100
200
300
X

each stroke of the microtome knife advances the position of the block face by 8 microns (8μ), the following relationship holds:

$$y = y_0 + n*8\mu$$

where y_0 is the fixed reference point.

We now attempt to fit a linear regression line,

$$y = a + bx$$

where a and b are the regression coefficients.

Table K displays the results of goodness of fit of data obtained from experiments I and II.

The compression error (C.E.) is defined as:

$$C.E. \quad (\%) = [(L_e - L_0)/L_e]*100 \qquad a1$$

where L_0 is the thickness of the section obtained (8 microns) and L_e is the length of block sectioned to yield one section.

Now, the equation

$$y = a + bx \qquad a2$$

expresses the relationship between the cumulative number of sections x obtained for a position y of the block face.

let L_y be the position of the block face before one section is cut. Then in accordance with the definition of L_e, $L_e + L_y$ would be the new position of the block face. Hence, from equation a2:

$$L_y = a + bx$$

Table K. Linear fit of data ($y=a + bx$) obtained from Experiments I and II to quantitate the compression error along the axis normal to the plane of cutting.

TABLE K

EXPERIMENT	χ^2 GOODNESS OF FIT TEST (P)	REGRESSION COEFFICIENT 'a' mm	REGRESSION COEFFICIENT 'b' $*10^{-2}$	STANDARD ERROR OF 'b' $*10^{-2}$	95% FIDUCIAL LIMITS OF 'b' $*10^{-2}$		PROBABILITY OF DIFFERENCE IN 'b' FROM EXPT. I & II
I	<.01	14.25	1.29	.01	1.33	1.25	.45
II	<.01	15.53	1.17	.06	1.35	0.88	

$$L_y + L_o = a + b(x + 1) \qquad a3$$

equations (a3) can be solved for L , resulting in

$$L_o = b$$

The regression co-efficient b represents the thickness of one section.

Using equation a1 the compression error is computed to be 37.89% and 34.45% for experiments I and II respectively.

B.3 Compression Error Along The Surface Of The Cut-Section.

The shrinkage in the lengths of the distances A, B, C is computed from their respective measurements before sectioning and after staining. The average shrinkage observed during each experiment constitutes the compression error. The shrinkage s is defined as the relative change in the distance between any two points. Hence,

$$s\ (\%) = [(L_s - L_h)/L_s]*100 \qquad c1$$

where, L_s is the distance between two points before the section is cut and L_h is the distance between the same points after staining and mounting on the histological slide.

The compression error (C.E.S.), in this case is:

$$C.E.S.\ (\%) = \frac{1}{n}\sum_{i=1}^{n} s_i \qquad i = 1 \ldots n \qquad c2$$

where n is the number of observations.

Using equations c1 and c2 the average compression error

along the surface of the sections was found to be 15.7% during experiment I and 10.18% during experiment II. An isotropic expansion of 10.18% is applied to all the sections to correct for the compression error in the plane of cutting.